Frictional Melting Processes in Planetary Materials: From Hypervelocity Impact to Earthquakes

John G. Spray

Planetary and Space Science Centre, University of New Brunswick, Fredericton, New Brunswick E3B 5A3, Canada; email: jgs@unb.ca

Annu. Rev. Earth Planet. Sci. 2010. 38:221–54

First published online as a Review in Advance on January 28, 2010

The *Annual Review of Earth and Planetary Sciences* is online at earth.annualreviews.org

This article's doi:
10.1146/annurev.earth.031208.100045

0084-6597/10/0530-0221$20.00

Key Words

comminution, fault lubrication, shock veins

Abstract

Frictional melting is the result of the conversion of mechanical deformation to heat under adiabatic conditions of slip. Within planetary materials, which are mainly natural ceramics, frictional melting occurs at high strain rates (typically $>10^{-2}$ s^{-1}) and at slip velocities greater than 0.1 m s^{-1}. The pathway to friction melting is controlled by the mechanical properties of a rock's constituent minerals, especially fracture toughness. Minerals with the lowest fracture toughnesses and breakdown temperatures are preferentially comminuted and fused to form the melt. The product is a polyphase suspension comprising mineral and rock fragments enclosed in a liquid matrix. This cools to form the rock type known as pseudotachylyte, and at even higher strain rates, it forms shock veins in meteorites and in impact craters, which may contain high-pressure mineral polymorphs. The generation of melt on sliding surfaces can lubricate earthquake faults, facilitate the post-shock modification of impact craters, and make landslides more hazardous.

1. INTRODUCTION

Frictional melting is an everyday process. The shiny, glazed tracks left in snow behind skis and on ice behind skates are illustrations that the sliding interface has been modified via friction-induced melting and water lubrication followed by rapid refreezing (Lind & Sanders 2004). The spinning of a vehicle tire on ice is an example of the hydrodynamic lubrication of the rubber-ice contact by frictional heating above 0°C (e.g., Zhang 2004). Rocky planetary materials can also melt by friction, although the temperatures involved for silicates are much higher than those of H_2O ice—typically above 1000°C. Planetary materials are also more complex because they are usually polyphase; that is, they comprise components with different melting points and physical properties. These variations control the pathway to melting by friction. Natural friction melts in planetary materials typically comprise a liquid matrix and entrained solid fragments of rock and minerals. During their formation they are polyphase suspensions, which can possess low viscosities and be highly mobile. Frictional melting as a process can exert control on coseismic earthquake dynamics and earthquake magnitude, landslide mechanics, and caldera lid deflation. In addition, it can facilitate the tectonic collapse of craters formed by hypervelocity impact. Frictional melting is an important transient phenomenon in planetary materials.

1.1. Historical Context

Natural polyphase friction melt cools to form what is referred to by geologists as pseudotachylyte (also spelled in Webster's dictionary as pseudotachylite; the original, former spelling is used here). This term was coined by Shand (1916) following his work on the Vredefort Structure of South Africa. Shand described anastomosing veins of dark rock that pervade leucocratic host Archean gneisses. This name alludes to the rock's similarity to "tachylyte," which is glassy basalt, and the prefix "pseudo" indicates that it is not a true basalt. Shand was at a loss to explain the origin of this unusual rock type but came close to understanding the mechanisms at play: "The form of the pseudotachylyte veins indicates that the granite was shattered by a sudden gigantic impulse or series of impulses" (page 216) and "the pseudotachylyte has originated from the granite itself through melting, caused not by shearing but by shock, or, alternatively, by gas-fluxing" (page 219). We now know that Vredefort is the world's largest known impact structure formed by the hypervelocity collision of a meteorite or comet with Earth (Martini 1978, Reimold & Colliston 1994, Spray 1998a, Earth Impact Database 2009) and that the pseudotachylyte developed there is the result of shock wave–materials interaction and ensuing large-displacement faulting (**Figure 1**).

Despite the fact that the type area for pseudotachylyte is an impact structure, much of our knowledge of frictional melting in terrestrial materials comes from studies of endogenic fault systems within Earth's crust, which is intrinsically linked to the earthquake process.

The earliest descriptions of what was to be known as pseudotachylyte predate the Vredefort studies. In the early nineteenth century, MacCulloch (1819) documented dark, anastomosing veins and dikes ranging from a millimeter to 2 meters in width of so-called trap rock pervading Archean gneisses along the eastern flanks of many of the islands of the Western Isles of Scotland (**Figure 2**). MacCulloch (1819) provides a description of the supposed trap rock's field occurrence on the island of Barra: "The trap veins are so numerous as to have separated the rock into small fragments, so that the whole has at first view the aspect of a conglomerate consisting of fragments of gneiss and granite imbedded in a basaltic paste" (page 83). Trap is a dark, fine-grained to aphanitic, hypabyssal to extrusive magmatic rock that is typically basaltic in composition. However, it does not normally carry significant clasts for much of its volume, as do the Western Isles examples. We now know that the so-called trap occurs predominantly within the Outer Hebrides thrust-fault

Figure 1

Pseudotachylyte type area: Vredefort impact structure, South Africa. The quarry face intersects a steeply dipping pseudotachylyte dike comprising a black matrix with rounded to subrounded inclusions of Archean granitoid gneiss. The inclusions are derived from the wallrock. The dike is approximately 5 m thick. Location: Leeukop Quarry, west of Parys. Photograph courtesy of Axel Wittmann.

system that was active during the Ordovician—a connection that alludes to the mechanical origin of the rock (Sibson 1975, Fettes et al. 1992, Kelley et al. 1994, Imber et al. 2002).

A half century later, King & Foote (1865, page 271), mapping in the Salem district of Madras in southeastern India, noted the presence of a ridge of hills defined by supposed trap dykes: "The rock is [charnockitic] gneiss of various kinds, altered, though more or less [in] immediate contact with trappean rocks, to such an extent and in such a manner that it is, as it were, very largely impregnated or shot with strings of dark-green or bluish-black compact trap, and on first seeing it, the term trap-shotten gneiss immediately occurred as a very appropriate one." Subsequently, Holland (1900) questioned the trap association for the breccias locally pervading the Salem gneisses, and instead favored the following view (page 201): "In these cases, therefore, where the rock has smashed along a particular band or line, the local rise of temperature resulting from the heat of friction is likely to be excessive; first, because of the limited area to which the disturbance is confined, and secondly, because this gives a primae facie evidence for supposing that the disturbance must have been unusually violent." Holland (1900) appreciated that the microtexture of these rocks was distinct from trap. Furthermore, he performed a simple experiment whereby he crushed some charnockite to a powder and heated it in a furnace to a white heat to produce "a fritted black cake having the lustre of tachylyte and showing in thin sections a black structureless matrix including angular fragments of quartz" (page 200). Holland's observations and deductions were prescient

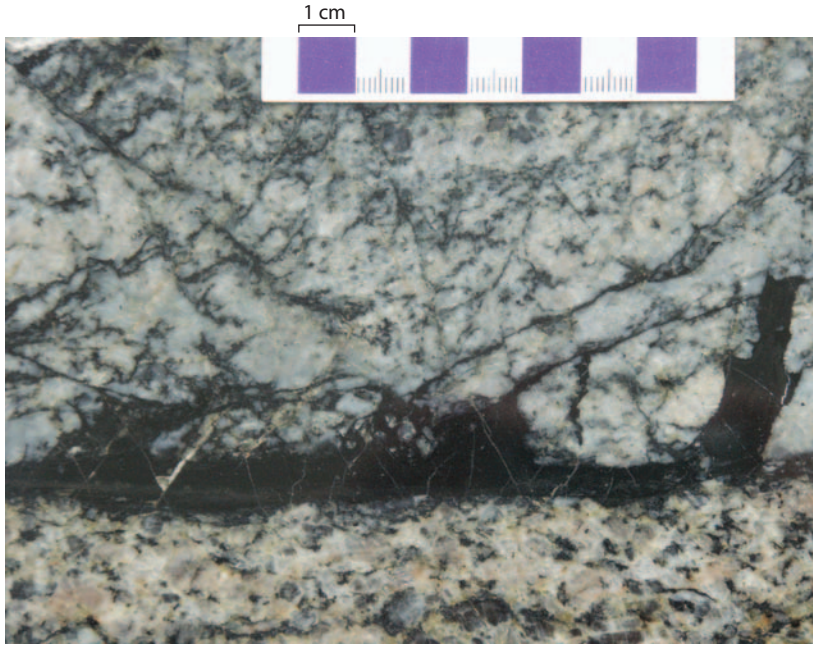

Figure 2

Friction melt (pseudotachylyte) developed in the Outer Hebrides fault system of NW Scotland. Note the more orthoclase-rich lower wallrock and more plagioclase-rich upper wallrock, as well as the injections off the main generation plane. Host rock is Archean gneiss.

given that high-resolution electron microscopy, subsequently used to resolve the microstructure and confirm the mechanical origin of pseudotachylyte, did not emerge for general usage by the science community for another 50 years. Moreover, he proposed a frictional origin for these rocks.

Pseudotachylyte is defined here as a rock that originates by frictional melting on a slip plane as a polyphase suspension comprising a once liquid matrix containing unmelted mineral and/or lithic clasts. Constrictions along the generating plane and injections of melt into wallrock fractures may filter out clasts to yield local melt-dominant zones. The matrix typically cools slowly enough to yield a microcrystalline to medium-grained igneous texture, depending on the original melt thickness and cooling conditions. The majority of pseudotachylytes do not comprise a glass matrix, even though many are aphanitic and glassy in appearance (hence the tachylyte allusion). It takes an electron microscope to resolve the nature of the matrix for pseudotachylytes that are a centimeter or less in width, which are typical of endogenic fault systems. Resolution of the matrix can be impossible in the field, even with the aid of a hand lens. This challenge can lead to considerable difficulty and an inability to distinguish pseudotachylyte from cataclasite, and especially from ultracataclasite. Having a debate on the outcrop about whether or not the matrix of such a fault rock was once molten then becomes academic in the worst sense! For some of the larger impact-generated pseudotachylytes—several tens of centimeters to meters wide and even thicker—the matrix crystals are typically phaneritic and can attain medium grain size (similar to the grain size of a diabase). Further diagnostic pseudotachylyte characteristics are discussed by Magloughlin & Spray (1992), Snoke et al. (1998), and Lin (2008).

An additional historical perspective concerns the terms flinty crush-rock and mylonite. Mylonite was originally used to describe rocks modified by the milling actions of crushing,

dragging, and grinding along thrust planes (Lapworth 1885), although a component of crystal-plastic behavior was intimated (Teall 1918). It is now understood that mylonites derive primarily by crystal-plastic grain-size reduction and syntectonic recrystallization rather than brittle processes (e.g., Bell & Etheridge 1973, White 1973, Mawer 1986, Passchier & Trouw 2005). Mylonite should therefore not be used in its original context. Flinty crush-rock was first used by Clough (1888) in his description of crushed granite from the Cheviot Hills of England. The term was subsequently deployed by Clough et al. (1909) in their description of rocks occurring in the ring faults associated with the Glen Coe cauldron subsidence of Scotland (Bailey & Maufe 1960). The relationship to crushing and shearing is clear and a mechanical origin is indicated, and these rocks have been reinterpreted as pseudotachylyte (Kokelaar 2007). So trap-shotten gneiss, flinty crush-rock, and certain apparent trap and tachylyte veins can be friction melts and encompassed by the term pseudotachylyte.

1.2. Purpose

This review adopts a mechanistic approach to understanding frictional melting in planetary materials. Planetary materials, at least for the terrestrial planetary bodies, are predominantly ceramics, although some asteroids are metals (the iron meteorites) or metal-silicate mixes known as pallasites (stony-iron meteorites). Here we focus on natural ceramics, which are largely represented by silicates. We explore the process of frictional melting in the context of material properties, fragmentation, strain rates, and slip scenarios. Slip scenarios include seismogenic faults, landslides, caldera collapse, and hypervelocity impact structures. Friction melts have also been reported from high-speed drilling (Killick 1990, Kennedy & Spray 1992) and rock-excavation operations (Spray 1989). Comminution is a critical mechanism in the pathway to frictional melting (Spray 1995), although some researchers previously considered fracture and fusion as unrelated processes, as debated by Wenk (1978) and Maddock (1983).

2. CONTROLS

The pathway to frictional melting is a complex one. It is a disequilibrium process whose critical events occur in seconds and even microseconds. The normal rules of producing molten material from rock do not apply (e.g., partial melting via burial or decompression). The key is to understand the controls exerted by materials behavior on heat generation. Frictional melting occurs under adiabatic conditions, unlike most geological processes, which take place in the isothermal regime. **Figure 3** summarizes various processes and products according to strain rate. The strain rate $\dot{\gamma}$ is defined as the velocity v (meters per second) of displacement of a material occurring within a specific width of deformation d in meters:

$$\dot{\gamma} = v/d \ \mathrm{s}^{-1}. \quad (1)$$

Figure 3 divides strain rates into subsonic (in which deformation occurs at velocities less than the sound-wave velocity for a given material) and supersonic (in which deformation occurs at velocities more than the sound-wave velocity for a given material). Most geological processes occur under subsonic conditions (e.g., steady-state plate movement, many earthquakes, volcanic events), whereas the upper end of seismogenic and shock-related effects are supersonic. Subsonic processes include mantle flow (i.e., bulk deformation) and delimited shear, as well as aseismic creep (i.e., localized/focused deformation). Comminution can also occur at higher strain rates under subsonic conditions. The strain rate is dependent on the width of the deformation zone as well as the velocity of displacement (i.e., the particle or material velocity). Representative widths

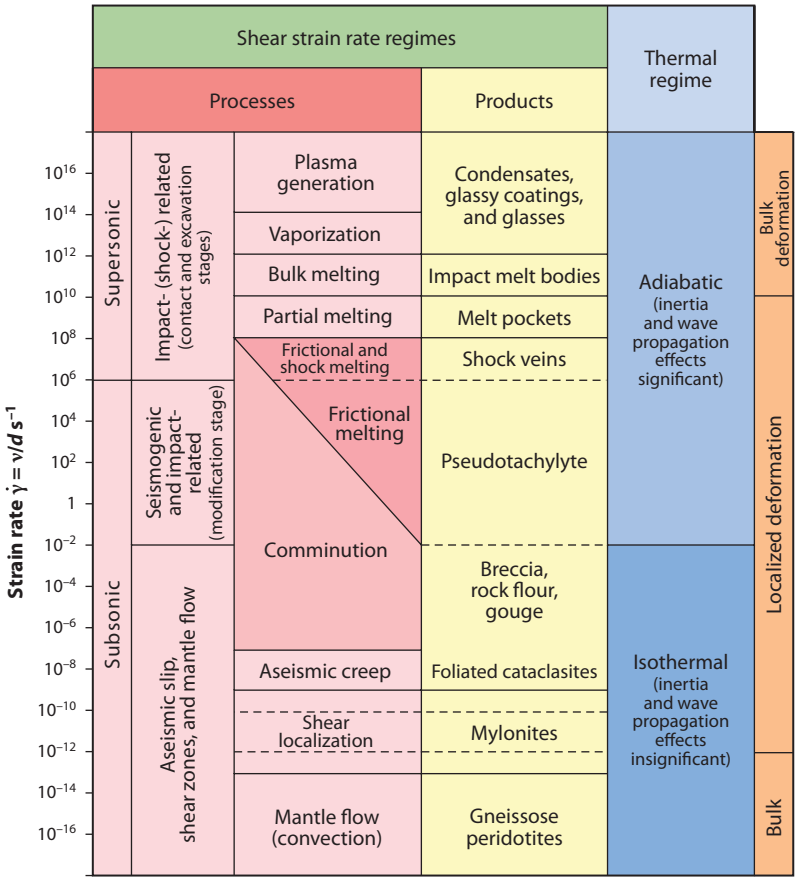

Figure 3

Strain rate $\dot{\gamma}$ and thermal regimes for natural ceramics with associated processes and products. v is the particle (material) velocity; d is the width of the deformation zone.

are tens of kilometers for mantle flow; <1 km for mid-crustal shear localization; <50 m for mid- to upper-crustal aseismic creep; <10 m for comminution and <10 cm for frictional melting, both typically occurring in upper-crustal endogenic fault zones; and <1 mm for melting in shock veins (**Figure 3**). There is a fundamental change in materials behavior at approximately $\dot{\gamma} = 10^{-2}$ (for ceramics), when the system evolves from isothermal to adiabatic. This means that heat generated by deformation is no longer shared with the surroundings, as it is under quasi-equilibrium conditions, but accumulates faster than it can be dissipated (i.e., there is negligible loss of heat via conduction to the cooler wallrocks). The accumulation of heat is responsible for a number of material changes, some of which can lead to melting. The first stage of the frictional melting process is comminution.

2.1. Comminution and the Comminution Limit

Comminution is the process of crushing and grinding a solid material to form smaller particles. For industrial applications, crushing refers to the larger size fractions (typically more than 1–10 cm in diameter), whereas grinding defines the processing of size fractions <1 cm in diameter (e.g., Lynch 1977). In fault systems, the product of comminution is referred to as rock flour or

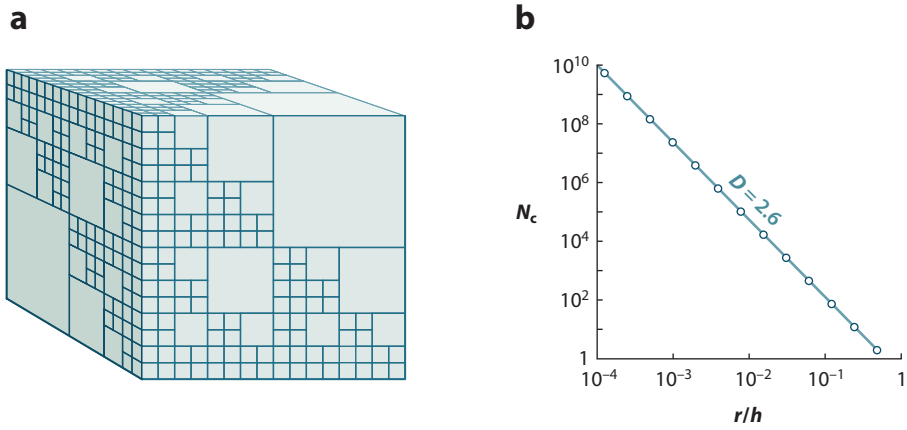

Figure 4

(*a*) Fractal cube, and (*b*) associated cumulative statistics with a fractal dimension D of 2.6. After Turcotte (1992).

gouge, or breccia for coarser products (>2 mm grain size). Cataclasis, as defined by geologists, is a process synonymous with comminution. However, the nouns cataclasite and ultracataclasite define originally powdered rocks that have been transformed into cohesive material. An additional (secondary) process is necessary to generate a cataclasite; this consolidation process can change the original texture, grain size, and grain shape of the gouge (e.g., via precipitation crystallization of binding mineral phases and Ostwald ripening). The cataclasite family of rocks should therefore not be confused with incohesive fragmental fault materials, although the former typically, in time, evolves from the latter (see Snoke et al. 1998 for an overview). In considering the comminution process here, we are concerned with the production of incohesive materials before any subsequent induration.

Comminution commonly results in a particle-size distribution represented by a large number of small fragments, an intermediate number of medium-size fragments, and a small number of large fragments. **Figure 4*a*** shows a fractal model for fragmentation adapted from Turcotte (1992) based on a master cube of volume h^3. Two diagonally opposed subordinate cubes are retained at each scale. During comminution, some cubes survive at each scale while others are fragmented. The largest contained fragment in the model has the dimension $r_1 = h/2$; successively smaller cubes have the dimensions $r_2 = h/4$, $r_3 = h/8$, and $r_4 = h/16$. The number N of cubes of each size for the whole three-dimensional master cube are $N_1 = 2$ (for r_1), $N_2 = 12$ (for r_2), $N_3 = 72$ (for r_3), and $N_4 = 1728$ (for r_4). We determine the fractal dimension D from:

$$D = \frac{1\mathrm{n}(N_{n+1}/N_n)}{1\mathrm{n}(r_n/r_n + 1)}. \quad (2)$$

The frequency-size distribution indicates a power-law relation, with a typical three-dimensional fractal dimension $D \approx 2.6$ for comminuted rock, as can be produced in a fault zone (e.g., Sammis et al. 1987). This is the fractal distribution for a discrete set. To compare this with statistical fractals obtained from actual fragmentation observations, we consider the cumulative number of cubes N_c (Turcotte 1992). The cumulative numbers are $N_{1c} = 2$ for r_1, $N_{2c} = 14$ for $r_1 + r_2$, $N_{3c} = 86$ for $r_1 + r_2 + r_3$, and $N_{4c} = 1814$ for $r_1 + r_2 + r_3 + r_4$. These cumulative statistics are shown in **Figure 4*b***, which is in agreement with

$$N_n = C/r_n^D, \quad (3)$$

Table 1 Power consumption for various ranges of industrial size reduction (from Lowrison 1974)

Method	Size Range	Energy Consumption (kW ton^{-1})
Coarse crushing	>10 cm	3–4
Intermediate crushing	1–10 cm	5–6
Fine grinding	125 μm	20–30
Superfine grinding	<125 μm	100–1000

where N_n is the number of cubes (fragments) with linear dimension r_n, C is a constant of proportionality, and D is the fractal dimension. If our fractal cube in **Figure 4*a*** has sides $r = 1$ m, then its unfractured parent would have a surface area of 6 m^2. If the fractal cube is fragmented according to the diagram in **Figure 4*a*** and disassembled, then its new surface area would be 54.75 m^2 (a ninefold increase). This illustrates the significant growth in surface area realized by comminution. This fractal model appears to work for both natural (e.g., the Lopez fault zone, San Gabriel Mountains, California; see Sammis & Biegel 1989) and laboratory-generated fault gouge (e.g., Biegel et al. 1989), with the fractal dimension $D \approx 2.6$ applying from micron to centimeter scales. This fractal dimension is not inclusive; different comminuted media can yield different values. For example, ash and pumice can possess $D = 3.54$ and artificially crushed quartz can possess $D = 1.89$ (Hartmann 1969). However, most fractal dimensions lie in the range $2 < D < 3$, and $D \approx 2.6$ is common for many fault-generated materials (e.g., Marone & Scholz 1989). Therefore, the associated fractal cube presented in **Figure 4*a*** is acceptable as an illustration of the scale-invariant nature of the comminution process, at least for relatively low strains (Sammis & King 2007).

The above scale-invariant relationship appears to falter when applied to the smaller fragment sizes (i.e., $\ll 1$ μm). The lower size bound has been referred to as the comminution limit or grind limit. This is the bane of mineral processing engineers. The relative amounts of energy consumed in industrial-scale size reduction reveal the difficulty of producing fine fragments (**Table 1**); the fact that fracturing smaller particles requires disproportionately more energy than fracturing larger ones is well known (e.g., Lowrison 1974). This supports the suggestion of von Rittinger (1867) that the energy consumed in the size reduction of solids is proportional to the new surface area produced. There are several possible explanations for the comminution limit:

1. A critical size volume of fragments is reached in which the smaller particles cushion and absorb the compressive and shear forces through relative movement (bulk yield) and cumulative elasticity, thus limiting further fracturing.
2. Below a critical particle size, cracks cannot nucleate and/or propagate under compression, and particles yield plastically instead of fracturing (i.e., the shear yield strength is grain size dependent below a certain threshold).
3. The smaller size fraction undergoes agglomeration to produce larger clusters, which define an apparent grinding limit (e.g., Knieke et al. 2009). Post-comminution grain growth in cataclasites may also eliminate the original smallest size fraction.
4. At high strain rates under adiabatic conditions, the generation of heat resulting from elastic and plastic particle deformation, coupled with a massive increase in surface area as comminution proceeds, leads to the melting of the finest particles, thus eliminating the smallest size fraction (Hirose & Shimamoto 2003, Ray 2004).

A characteristic of comminution is its inherent inefficiency with respect to generating new surface area (Beke 1964). Industrial crushing methods as part of mineral beneficiation processes are, at best, 1–2% efficient based on the absolute ratio of energy required to generate new surface area relative to the total mechanical energy input (Tromans 2008). This means that 98–99% of

the energy is expended in processes other than size reduction. The bulk of this energy goes to heat in the conversion of mechanical energy. Because of this, the milling of rock must be controlled so that operating temperatures do not reach the melting points of the feed material or equipment.

Notwithstanding the above, the critical size defining the comminution limit has evolved over the past several decades: It has tended to decrease (from micron to submicron). Technology has facilitated our ease of observation and analysis of materials at increasingly higher resolution. The nanometer scale is now within easy reach. This means that, at least for some reported cases, the comminution limit may be more apparent than real. Yund et al. (1990) describe submicron crystalline fragments resolvable via transmission electron microscopy to 10–15 nm, along with 5–60% amorphous material, in laboratory-based friction experiments on Westerly granite. Chester et al. (2005) observed natural ultracataclasite comprising particles <100 nm in size in the Punchbowl Fault of the San Andreas system (although it should be noted that this is an evolved fault rock, which has undergone secondary modification). Nevertheless, a crushing limit does appear applicable in many cases. Moreover, the critical particle size is strength dependent and hence material dependent.

Numerous researchers have explored the comminution limit (e.g., Kendall 1978, Hagan 1981, Sammis & Ben-Zion 2008). Application of the Griffith energy criterion of fracture to an idealized geometry indicates that the propagation stress required to activate a flaw is inversely proportional to the square root of sample size. Because the flaw length is limited by the particle size, strength increases as the inverse square root of particle size. This reveals a critical particle size below which crack propagation is seemingly impossible under compressive forces. The increase in strength is then ultimately limited by plastic yielding. Hagan (1981) proposed that the critical particle size is controlled by the conditions for crack formation or nucleation, rather than crack propagation. He calculates, for example, that the critical size for the brittle-ductile transition is 0.5 μm for soda-lime glass, 3.3 μm for Al_2O_3, and 1.1 μm for SiO_2—results three times smaller than those Kendall (1978) calculated based on crack propagation. Nevertheless, compressive loading does not appear to produce particles significantly smaller than 1 μm, so the existence of particles in the nanometer-size range requires explanation. Three possibilities include (*a*) shock loading in the supersonic field (**Figure 3**), whereby stresses can be as much as 50 times higher than the flow stress (Meyers 1994), thus reducing the brittle-ductile transition (i.e., there is minimal shear strength); (*b*) subcritical crack growth, whereby stress corrosion can reduce the fracture toughness by 80% (Atkinson 1984), thus facilitating crack growth at much lower stresses; and (*c*) fragmentation by tensile rather than compressive failure (Sammis & Ben-Zion 2008).

The comminution process is controlled by the mechanical properties of the materials being crushed. For rocks and minerals, these properties include the yield strength, shear yield strength, fracture toughness, and thermal conductivity. We shall consider each in turn.

2.2. Relations Among Mohs Number, Yield Strength, and Shear Yield Strength

Solid planetary materials, represented by minerals, can display a wide range of physical properties. The majority can be classified as ceramics, which possess certain common traits: brittleness (low fracture toughness), low tensile strength, and high compressive strength compared with other materials (e.g., metals and their alloys). One property that can be linked to strength is Mohs number. The scratch resistance of minerals is customarily defined by geologists, lapidaries, and gemologists using Mohs scale H_M (Mohs 1825), which ranges from 1 (represented by talc) to 10 (uniquely represented by diamond). Whereas some minerals show marked variation in H_M depending on crystallographic orientation (e.g., kyanite, calcite, diamond), most minerals show negligible individual anisotropy such that their identification can be assisted by a single scratch

test. However, there can be variation in H_M within a given mineral group owing to solid-solution and substitution effects; typically this is within 10–20%. The Mohs scale is qualitative and does not exhibit a linear increase in hardness with number (Hodge & McKay 1934, Knoop et al. 1939). It does not afford comparison with strength properties for nongeological materials in terms of providing broader context. However, Taylor (1949) and Tabor (1954) revealed that Mohs number can be approximately related to the indentation hardness H_I (true hardness) through

$$(nH_M)^3 = H_I, \tag{4}$$

where n ranges between 1.3 and 1.6, except for the extremes of the scale. The indentation hardness (true hardness), H_I, is defined by the load divided by the projected area of the indentation (also known as the Meyer hardness number). More recently, Broz et al. (2006) defined the power-law relationship:

$$0.123\, H_M^{2.3} = H_I. \tag{5}$$

Ignoring correction factors for the effects of work hardening, the yield strength σ_y and shear yield strength k can be derived from (Meyers & Chawla 2009):

$$H_I \approx 3\sigma_y \approx 6k. \tag{6}$$

A more comprehensive treatment of plastic deformation requires determination of maximum and minimum stresses (Tresca yield criterion) or all three principal stresses (von Mises yield criterion). These characterize deviatoric stresses, which are important in driving shear-deformation processes (Green 1998). For simplicity, minerals are considered here in terms of uniaxial behavior. **Figure 5** shows that, under prefailure (prefracture) conditions and under the appropriate temperature-pressure conditions, minerals with the lowest H_M, σ_y, and k values can facilitate creep behavior in fault systems if present in sufficient volume. **Figure 5** also relates bond type to these properties for the minerals shown. Covalently bonded minerals are the strongest, followed by ionic, ionocovalent (the majority of silicates), and lastly, ionocovalent combined with van der Waals. The occurrence of weak phyllosilicates (e.g., talc) at 3-km depth in the San Andreas Fault system provides a good example of low-k materials behavior facilitating creep rates as high as 28 mm year^{-1} (e.g., Moore & Rymer 2007). At higher strain rates, the fracture toughness K_C controls the failure mechanism in fault systems; comminution dominates under these conditions.

2.3. Fracture Toughness

As materials with large lattice resistances, ceramics are brittle and possess fracture toughnesses that are approximately one-fiftieth of those shown by ductile metals. This is because of the covalent (e.g., SiO_2), ionic (e.g., TiO_2), and ionocovalent (e.g., Mg_2SiO_4) bonding and the resulting localized electron distribution of ceramics versus the "sea" of delocalized electrons characteristic of the metallic bond (**Table 2**, **Figure 6**). Among natural ceramics, covalent minerals exhibit the highest fracture toughnesses (e.g., diamond, SiC, Al_2O_3), followed by ionic (e.g., metal oxides), then ionocovalent (e.g., silicates) phases. Ionocovalent minerals combined with van der Waals bonds (i.e., many phyllosilicates) possess the lowest fracture toughnesses. This trend is comparable with that shown for yield strength and shear yield strength in **Figure 5**. Quartz is included here with the oxides rather than the tectosilicates, as its mechanical behavior is distinct from the feldspars even though their crystal system is shared (**Figures 5** and **6**). Fracture toughness is defined by the critical stress intensity factor:

$$K_C = \sqrt{EG_C}, \tag{7}$$

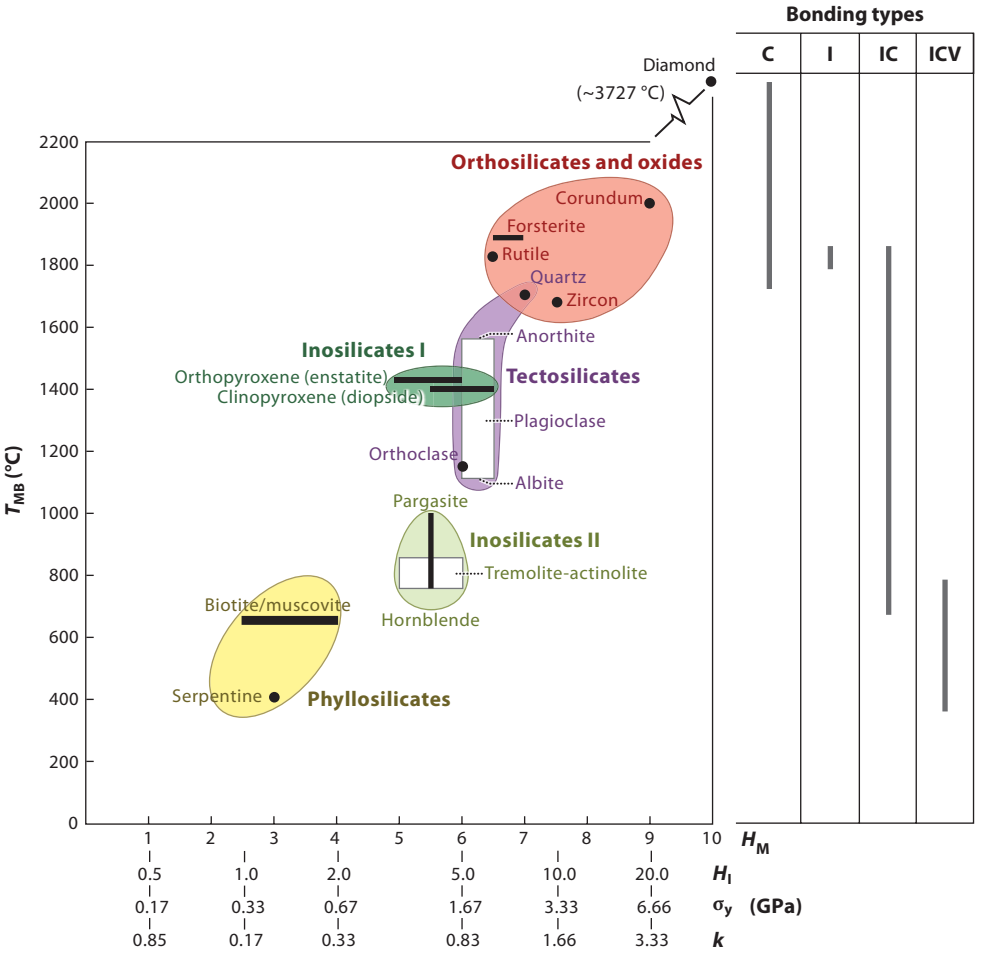

Figure 5

Approximate melting or breakdown temperature T_{MB} versus Mohs number H_M, indentation hardness H_I, yield strength σ_y, and shear yield strength k for selected minerals. See **Table 2** for data source. Inosilicates I refers to single-chain inosilicates, and inosilicates II refers to double-chain inosilicates. Bonding types: C, covalent; I, ionic; IC, ionocovalent; ICV, ionocovalent with van der Waals.

where E is Young's modulus and G_C is the toughness. Under conditions of fast fracture, K_C is equivalent to the stress intensity factor

$$K_C = K_{IC} \tag{8}$$

and

$$K_{IC} = \sigma\sqrt{\pi a}, \tag{9}$$

where σ is the stress and a is the crack size (Meyers & Chawla 2009). Most ceramics have fracture toughnesses in the range of 0.1–3.0 MPa m^{-2} (diamond is an exception, attaining 5 MPa m^{-2}), compared with 5–200 MPa m^{-2} for metals. Natural ceramics contain inherent cracks and flaws; these, combined with K_C, control their strength (at least down to a grain size of 1 μm). Even at the crack tip, where the stress is intensified, the lattice resistance in ceramics makes slip difficult,

Table 2 Physical properties of selected minerals based on data from Horai (1971), Bradt et al. (1973), Deer et al. (1992), Spray (1992), Clauser & Huenges (1995), Tromans & Meech (2002), Broz et al. (2006), and Whitney et al. (2007)

			Melting or breakdown temperature	Mohs number	Indentation hardness	Yield strength	Shear yield strength	Fracture toughness	Thermal conductivity
			T_{MB} °C	H_M 1–10	H_I GPa	σ GPa	k GPa	K_{IC} MPa m^{-2}	λ W m^{-1} °C^{-1}
Phyllosilicates	mica	muscovite	650	2½–4	1–2	0.33–0.66	0.16–0.33	0.2	2.5
		biotite						–	1.7
	serpentine	chrysotile	400	2½	—	—	—	—	5.3
		lizardite	400		—	—	—	—	2.3
		antigorite	500	2½–3½	—	—	—	—	3.0
		serpentine (undefined)	400	2½	1.2	0.4	0.2	—	~3.0
Sorosilicates	$Ca_2FeAl_2Si_3O_{11}(OH)_2$	epidote	500	6	—	—	—	0.02–0.20	2.9
Inosilicates I	pyroxene	enstatite	1425	5–6	3.4–5.0	1.13–1.66	0.57–0.83	–	4.4
		diopside	1400	5½–6½	4.5–6.5	1.5–2.16	0.75–1.08	–	5.4
		jadeite	800	6				0.7	5.6
Inosilicates II	amphibole	actinolite	750	5 – 6	3.4–5.0	1.13–1.66	0.57–0.83	0.76	4.2
		tremolite	850					–	4.8
		hornblende	750	5½	4.5	1.5	0.75	–	2.8
		pargasite	1000					–	—
Tectosilicates	feldspar	albite	1100	6–6½	6	2	1	–	2.3
		anorthite	1550					0.75	1.7
		orthoclase	1150					0.9–1.3	2.3
	SiO_2	quartz	1730	7	12	4	2	1.6–2.4	7.2

Orthosilicates	olivine	forsterite	1900	6½–7	6.5–8.4	2.2–2.8	1.1–1.4	–	5.0
		fayalite	1900						3.1
	Al_2SiO_5	andalusite	1600	6½–7½	10	3.3	1.65	1.6	7.6
		sillimanite	1400		11	3.7	1.83	1.8	9.0
	$Al_2SiO_4(OH,F)_2$	topaz	1000	8	18	6	3	1.0	~11
	garnet	Fe-Mg-rich	1200	6–7½	15	5	2.5	1.4–1.6	–
		Ca-rich	1200		13	4.3	2.15		–
	$ZrSiO_4$	zircon	1695	7½	10	3.3	1.65	–	2.6
Oxides, etc.	$CaCO_3$	calcite	900	3	1.5	0.5	0.16	0.4	3.6
	TiO_2	rutile	1850	6½	6.5	2.2	1.08	2.3	5.6
	Al_2O_3	corundum	2000	9	20	6.6	3.3	2.4–2.8	25
	Fe_2O_3	magnetite	1600	5½–6½	–	–	–	1.75	5
	C	diamond	3727	10	115	38	19	5	70

promoting brittle (fast) fracture. In contrast, crack-tip plasticity in metals provides for an energy-absorbing plastic zone that inhibits crack propagation and engenders high toughness, which results in failure by creep (ductile) fracture (except at very high strain rates). Ceramics possess high compressive strengths, typically eight times larger than their tensile strengths (Meyers & Chawla 2009). This means that their failure typically occurs under tension. Fracturing and fragmentation can proceed during conditions of bulk compression arising from the development of localized regions of tension. Cracks initiate and propagate (in mode I) in ceramics via the development of microregions of tension, which result in axial splitting and spalling under bulk compression. The main strength control is the number and length of microcracks; variability in these values results in many ceramics showing a standard deviation of up to 25% in their tensile strengths (Ashby & Jones 2005a).

The K_C data for minerals remain relatively limited, although the advent of new microhardness and depth-sensing indentation measurement techniques (e.g., Broz et al. 2006) as well as theoretical determinations (e.g., Tromans & Meech 2002) have improved the database in the past decade (**Table 2**).

The temperature dependency of the fracture strength of polycrystalline rocks is negligible between 25 and 600°C (Davidge 1979); temperatures above this will tend to render the crack tip more plastic and thus increase the fracture toughness. Ultimately, creep conditions will dominate when temperatures attain $T > 0.4$ to 0.5 T_M (where T_M is the material melting point in degrees Kelvin), whereupon shear strength behavior will dominate (**Figure 5**). At the other extreme, it has been shown that subzero temperatures can lower the fracture toughness: Industrial-scale cryogenic grinding using liquid nitrogen (at −196°C and below) is deployed to facilitate embrittlement of materials so that they can be ground more effectively during mineral beneficiation processing (e.g., Wilczek et al. 2004). Notwithstanding certain temperature and pressure influences, the mechanical response of planetary materials is critically dependent on the strain rate (e.g., Kipp et al. 1980): In the adiabatic regime (i.e., strain rate $>10^{-2}$ s), fast fracture is likely to dominate the mechanical response of minerals and rocks, even at high temperatures.

Within the fast fracture regime, the strain-rate dependency of fracture toughness is not well understood. The dynamic fracture toughness K_{ID} is a function of the pulse duration, unlike the static stress intensity factor K_C. For example, Ravi-Chandar & Knauss (1984) show that fracture toughness increases with a decrease in load-application time for durations of 50 μs or less, but for longer durations the fracture toughness is found to be independent of time. Suresh et al. (1990) conclude that the dynamic fracture toughness in brittle materials is higher than the static fracture toughness owing to a loss of stiffness ($K_{ID}/K_{IC} = 1.1$–1.4). This means that the fracture toughnesses reported in **Table 2** and **Figure 6** are underestimates for the adiabatic thermal regime, especially for shock conditions (discussed below).

Experimental evidence indicates that fracture strength increases with confining pressure for polycrystalline rocks owing to the closure of cracks and joints, although this may not affect individual mineral response (Mogi 1974). Crack location also has an influence on fracture toughness. Tromans & Meech (2002) determined that fracture toughness values for high-angle grain-boundary cracking in pure single-phase minerals are less than those for intragranular cracking by 10–14%.

Figure 6 shows fracture toughness K_{IC} versus melting/breakdown temperature relations for selected minerals. There is a general positive relationship between K_{IC} and T_{MB} with the more refractory phases possessing higher values of K_{IC}. As with relations between shear strength and T_{MB}, the toughest minerals are orthosilicates and certain oxides, followed by tectosilicates, inosilicates, and phyllosilicates. This means that there is a hierarchy of response to comminution, whether it be in a fault zone or an industrial ball mill.

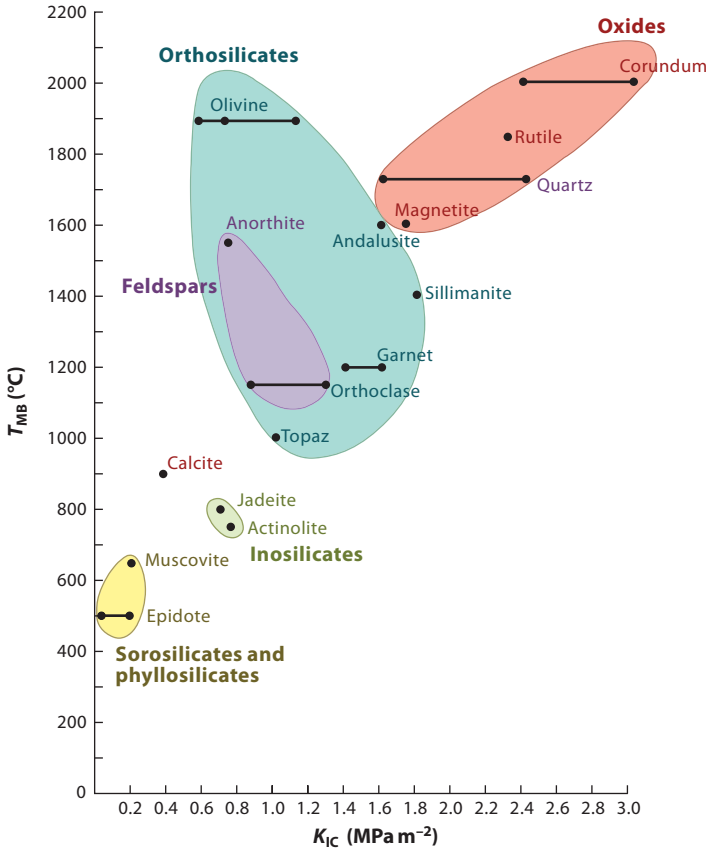

Figure 6

Approximate melting or breakdown temperature T_{MB} versus fracture toughness K_{IC} for selected minerals. Data from **Table 2**.

2.4. Relations Among Thermal Conductivity, Thermal Shock, and Decrepitation

Figure 7 shows relations between thermal conductivity λ and melting-breakdown temperature T_{MB} for selected minerals. Most minerals have λ values of 1.5–8.0 W m^{-1} °C^{-1}, which means that they are poor heat conductors. (Metals and their alloys have typical λ values of 50–250 W m^{-1} °C^{-1}; i.e., they are good heat conductors.) More conductive minerals (not shown) include topaz (λ ≈ 11 W m^{-1} °C^{-1}), corundum (λ ≈ 25 W m^{-1} °C^{-1}), and diamond (λ ≈ 70 W m^{-1} °C^{-1}). Aside from these outliers, which do not constitute major rock-forming phases, most minerals exhibit limited variation in λ, and there are no significant trends relative to T_{MB}, σ_y, k, and K_C. Some orthosilicates and oxides do show higher conductivity values, and feldspars, along with some phyllosilicates, show lower values (**Figure 7**). There is also some variation in values for given minerals reported in the literature (e.g., Horai 1971, Clauser & Huenges 1995); this is most likely attributable to compositional differences resulting from substitution (e.g., solid solution effects) and/or "contamination" by inclusions, as well as the possibility of interlaboratory discrepancies. The values shown (**Table 2** and **Figure 7**) are for determinations made at 20–25°C; it has been shown that most minerals exhibit decreasing thermal conductivity with increasing temperature (Clauser & Huenges 1995).

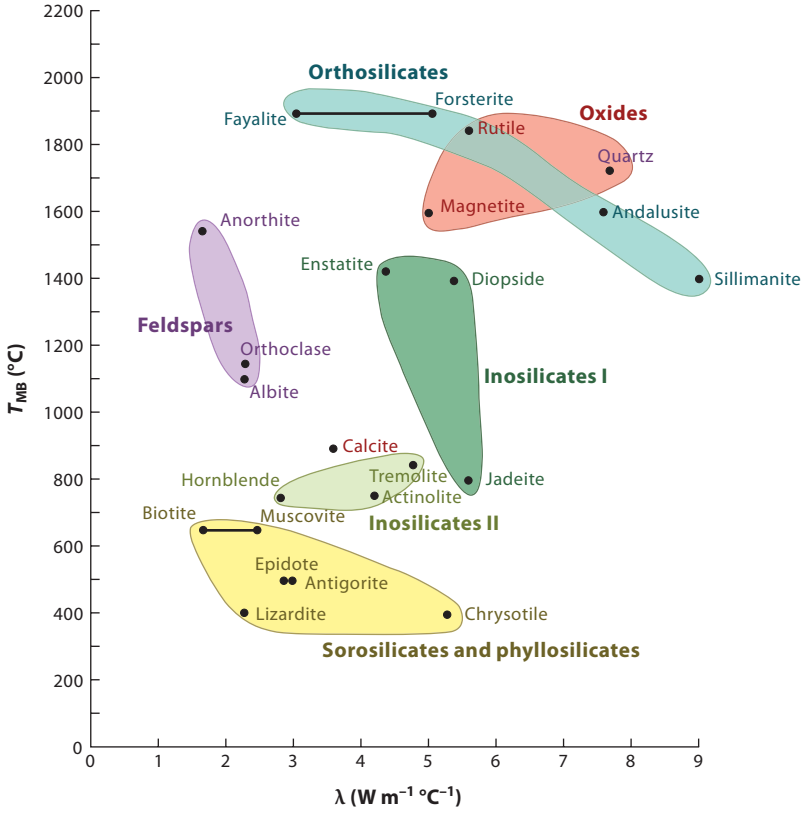

Figure 7

Approximate melting or breakdown temperature T_{MB} versus thermal conductivity λ for selected minerals. Data from **Table 2**.

The thermal conductivity values for the majority of minerals lead to some important consequences under adiabatic conditions of deformation. Heating of a poor heat conductor creates internal (intragrain) and near-neighbor (intergrain) stresses. Rapidly imposed thermal strain on the order of a few percent can result in fracture (e.g., Green 1998). The effect will apply during frictional heating and especially once partial melting has taken place: Solid clasts and wallrock will then be juxtaposed with hot (typically 1000°C or more) silicate liquid. Thermal shocking can lead to decrepitation, which is the spontaneous shattering of a solid resulting from the imposition of steep, nonlinear thermal gradients. This mechanism of shattering in minerals can be brought about by differential thermal expansion (within and between grains), dehydration of chemically bound volatile species (e.g., in micas and amphiboles), phase changes (e.g., α to β quartz), and evaporation of trapped adsorbed and absorbed volatiles and fluid inclusions. Extreme differential thermal expansion can result in onion-ring exfoliation, which reduces fragment size. Volatile heating can induce fragment explosion. Phase changes can impart intra- and intergrain stresses that result in fracture. All these decrepitation effects take place as a result of heat: They are secondary thermal fragmentation mechanisms following initial comminution and associated primary mechanical fragmentation. Although the thermal conductivities of minerals are inherently low, the relatively higher thermal conductivity of the important rock-forming mineral quartz, along with its relatively high fracture toughness and yield strength, contribute to its survival as a clast in many

friction melts derived from quartz-bearing protoliths. This is assisted by the enhanced radiative (photon) transfer that occurs at red heat (500–1000°C) in translucent to transparent minerals such as SiO_2 (e.g., MacPherson & Schloessin 1982).

Equipped with a basic knowledge of high-strain-rate materials behavior for natural ceramics, we can now explore how comminution leads to frictional melting.

3. THE PATHWAY TO FRICTIONAL MELTING

The pathway to frictional melting of planetary materials can start with one of several scenarios: (*a*) fast fracture, fracture propagation, and slip in the upper crust within intact material; (*b*) failure of an existing slip/damage zone in the upper crust; and (*c*) ductile fracture in the middle crust under nominally plastic conditions (e.g., the evolution of adiabatic shear bands into cracks under conditions of increasing strain rate). All three scenarios may be present in the same fault complex and may occur along a common failure plane at different locations. Typically, scenarios (*b*) and (*c*) may lead to scenario (*a*) if they generate new fracture surface(s). We are not concerned here with deeper subduction-related earthquakes, which may involve various complicating phase transitions, but rather effects in the upper and middle crust.

The prelude to slip that leads to an earthquake is of considerable interest, and much rock mechanics literature is devoted to understanding this phase (i.e., premonitory behavior), especially literature pertaining to laboratory studies (e.g., Marone 1998, Beeler 2006). Most of these experiments have been performed at strain rates of 10^{-7}–10^{-4} s^{-1} (**Figure 3**). Until the advent of large displacement (>1 m), high-speed (>1 m s^{-1}) rotary friction apparatus, most experiments could not adequately simulate coseismic behavior. Here we are specifically concerned with the coseismic phase and associated dynamic weakening mechanisms. Our start scenario is a preexisting fracture surface that undergoes slip. This occurs in the adiabatic thermal regime at strain rates greater than 10^{-2} (**Figure 3**) and at slip velocities that are typically greater than 0.1 m s^{-1}.

3.1. Comminution–Frictional Melting Transition

From our basic understanding of the physical properties of the common rock-forming minerals, as discussed in Section 2 above, it is clear that there is a hierarchy of response to their mechanical behavior. At the onset of slip, there may be some governance of mineral behavior according to yield strength and shear yield strength (**Figure 5**). In order of increasing values, this starts with phyllosilicates and moves through double-chain inosilicates to single-chain inosilicates, tectosilicates, orthosilicates, and oxides. A similar order is shown in the melting/breakdown temperature T_{MB}, although orthoclase and more sodic plagioclase melt before the single-chain inosilicates. However, whereas this hierarchy may control creep (e.g., aseismic behavior in fault/shear systems) and ductile fracture, the rapid acceleration to coseismic strain rates on the slip zone will force comminution by fast fracture. Mineral response under these conditions is controlled by fracture toughness K_C (**Figure 6**). The preferential comminution of phases with lower fracture toughnesses results in an increase in their surface area concomitant with size reduction. This leads to the multiplication of elastic and plastic particle deformation through myriads of grains such that heat accumulates preferentially in the finest fraction. At these strain rates, heat cannot be removed by conductive or convective cooling. This is the adiabatic regime, so the temperature increases to T_{MB}. Frictional melting of the finest fraction can thus account for an apparent comminution limit (as discussed in Section 2.1). Once the melt attains sufficient volume, slip-zone lubrication can occur.

A number of important conclusions can be drawn from this sequence of events. First, minerals comminute and melt in specific order depending on the nature of their crystal structures and

bonding. There are common responses shown by groups of minerals in this respect. Second, frictional melting is a nonequilibrium process, so eutectics and minimum melts do not form (unlike in many igneous processes). Rather, melting proceeds according to the individual melting points of minerals. Bulk melting is rarely achieved. A consequence of this melting hierarchy is that if phyllosilicates (e.g., micas) and/or double-chain inosilicates (amphiboles) are present in a rock, then the resulting melt will be enriched in those components, leaving the more refractory phases as clasts. This means that for polyphase rocks undergoing frictional melting, the composition of the molten matrix is typically more ferromagnesian and basic than the bulk rock. With this model in mind, we now proceed to consider a case study, that of frictionally melting Westerly granite using axial friction-welding apparatus.

4. HIGH-SPEED LABORATORY SIMULATIONS: CASE STUDY

4.1. High-Speed Friction Apparatus

The deployment of rotary friction machines in the laboratory has afforded realistic slip rates and displacements that simulate the coseismic phase of the earthquake cycle. One of the earliest uses of rotary apparatus was by Erismann et al. (1977) in their simulation of the Kofels landslide. Following this, industrial friction-welding apparatus involving orbital (Spray 1987), radial (Spray 1988), and axial (Spray 1993, 1995) configurations were adapted for rock studies. This application grew out of the development of novel welding techniques for the joining of similar and dissimilar metals and plastics for the industrial manufacturing sector (e.g., Fletcher 1972). Friction welding is typically achieved by rotating the material to be joined against a stationary counterpart under load until sufficient heat is generated to soften and bond the interface. In the case of metals and their alloys, friction welding does not cause melting; rather, it causes plastic and superplastic behavior via adiabatic shear and drag-controlled plasticity when T exceeds 0.3–0.4 T_M, the melting temperature in degrees K (Ashby & Jones 2005b). Subsequent modifications for rock applications have included enhanced computer control and monitoring to microsecond resolution, fast-response optical pyrometry, and high-precision velocity and pressure sensing (Spray 2005). Development in Japan of an in-house, rotary-shear, high-speed friction machine has complemented the results obtained from friction-welding apparatus (e.g., Shimamoto & Tsutsumi 1994, Tsutsumi & Shimamoto 1997, Lin & Shimamoto 1998, Di Toro et al. 2006a,b). Here we cite as a case study the results of a high-speed slip experiment on Westerly granite using modified axial friction-welding apparatus.

4.2. Frictional Melting of Westerly Granite

The experiment involves rotating a 3.65 cm–diameter, 7 cm–long cylinder of machined Westerly granite against a stationary counterpart at a start velocity of 3.5 m s^{-1} at a load of 400 N. Friction between the two faces results in deceleration and eventual stoppage after 3 s. The mean velocity over the duration of the run is 1.8 m s^{-1} for a total displacement of 5.4 m. This simulates coseismic slip and displacement values recorded for a natural seismogenic event resulting in a large earthquake (e.g., Scholz 2002). Further details of the experimental procedure are given in Spray (2005). During the initial contact phase, some material is lost from the interface as comminuted material is centrifugally ejected, but then the interface glows bright red and further loss is minimal. An approximate coefficient of dynamic friction μ_k is derived from the theoretical formula of Bowden & Tabor (1950):

$$\mu_k = \frac{(T - T_o)(J\pi r)\sqrt{2q\lambda r}}{\alpha W g v}, \tag{10}$$

where T is the temperature of the sliding interface, as measured by an optical pyrometer; T_o is room temperature (25°C); J is the mechanical equivalent of heat (4186 J kg^{-1}, used for calorie-to-joule conversion); r is the effective sample radius (16 mm for open friction runs, 15.5 mm for closed runs); α is the fraction of heat partitioned into each face (for the purposes of this work $\alpha = 1$ because the interfaces remain in constant contact); W is the load (in Newtons), as measured by the load sensor; g is the acceleration resulting from gravity (9.81 m s^{-2}); v is the velocity (as measured by the digital encoder, in meters per second); λ is the thermal conductivity (3.0 W m^{-1} °C^{-1} for granite); and q is the heat-transfer coefficient, which relates to heat loss by emission assuming Newton's law of cooling (a value of 0.17 mW m^{-2} °C^{-1} is used here).

Figure 8*a* shows the calculated kinetic coefficient of friction μ_k versus acceleration. The blue-colored sections of line indicate strong deceleration with increasing friction; the red indicate reduced deceleration, and even a brief phase of acceleration, with decreasing friction. We correlate

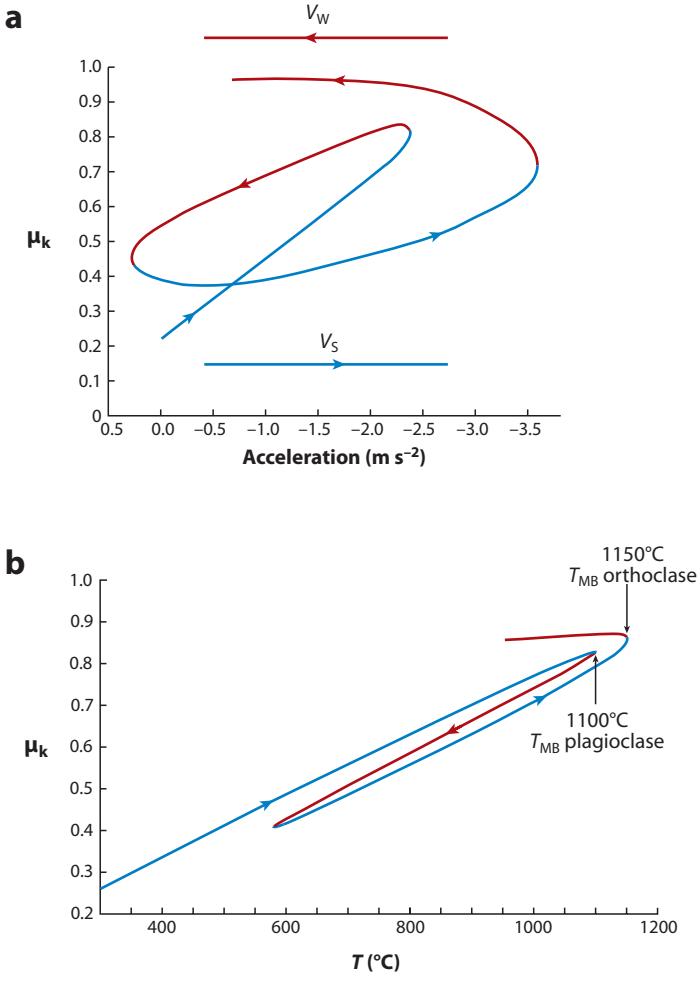

Figure 8

Calculated kinetic coefficient of friction μ_k versus (*a*) acceleration, and (*b*) temperature for the Westerly granite friction experiment. V_s = velocity strengthening; V_w = velocity weakening.

Table 3 Modal mineralogy of Westerly granite used in the case study. Also shown are values for volumes of minerals assigned to the fractal cube of Figure 9

Mineral	Percentage Volume of Rock	Percentage Volume of Fractal Cube	T_{MB} °C	K_{IC}
Quartz	39%	46%	1713	2.4
Orthoclase	20%	20%	1150	1.0
Plagioclase	26%	20%	1100	0.8
Mica	11%	14%	650	0.2
Accessories	4%	0%	various	various

the blue-line behavior with boundary lubrication (comminution) and velocity strengthening (V_s) and the red line with hydrodynamic lubrication and velocity weakening (V_w). These effects have been explored theoretically by Brodsky & Kanamori (2001). **Figure 8*b*** shows the calculated kinetic coefficient of friction versus temperature. The blue sections show increasing temperature up to 1100–1150°C with increasing friction, whereas the red sections reveal a temperature decrease with decreasing friction. We now attempt to link these experimental results with the composition of Westerly granite in terms of its constituent minerals.

Table 3 summarizes the modal mineralogy of the studied granite sample, as well as mineral melting or breakdown temperatures. Westerly granite comprises quartz, orthoclase, plagioclase ($An_{<20}$), and biotite. Chlorite, epidote, titanite, zircon, apatite, and opaques constitute minor components but are not considered to influence the mechanical behavior of the rock during comminution and melting owing to their small volume. We can see from examining **Figure 6** that the lower T_{MB} and K_{IC} values for mica result in this phase undergoing preferential comminution, thermal breakdown, and melting, followed by the feldspars and the quartz. We now return to Turcotte's fractal cube of volume h^3 that is representative of comminuted material with a fractal dimension of 2.6 (**Figure 4**). **Figure 9*a*** shows the same fractal cube but with the appropriate minerals assigned for Westerly granite. The blue cubes represent the tougher quartz, which occur as the largest fragments ($h/2$ cubes = 25% volume) as well as half of the smallest $h/16$ cubes (21% total volume). Plagioclase and orthoclase are combined in the purple cubes as feldspar; they are assigned all the $h/4$ cubes (19% volume) and the remaining half of the smallest cubes (21% volume). The yellow cubes ($h/8$ = 14% volume) represent mica (mainly biotite with some muscovite). The percentage volumes roughly correspond to those determined from Westerly granite (**Table 3**).

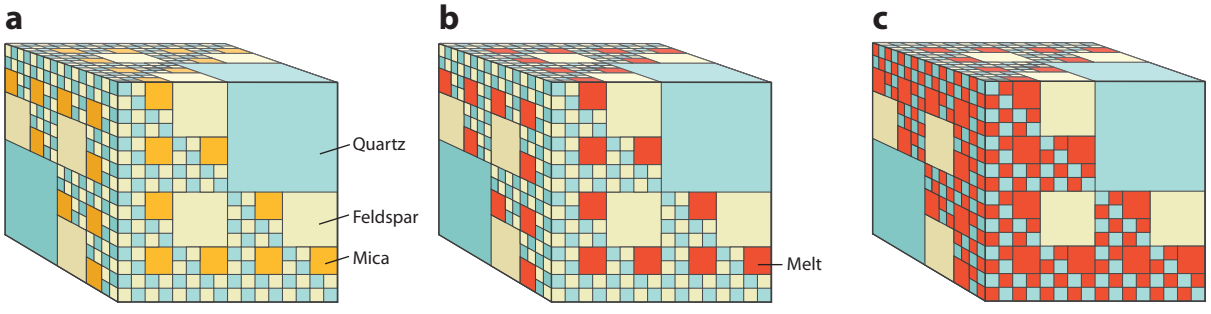

Figure 9

(*a*) Assignment of Westerly granite mineral modes to the fractal cube. (*b*) Biotite melted (*red cubes*). (*c*) Biotite and 50% feldspar melted (*red cubes*).

The fractal cube constructed this way is merely a static representation of the relative volumes and sizes of the major minerals, with some inference regarding their size distribution. In reality, as comminution proceeds, the mineral particles would be constantly moving as well as changing their shapes and sizes. During the initial slip and comminution phase, all the mica undergoes breakdown (dehydration) and melts to yield 14% melt volume (**Figure 9*b***). This amount is sufficient to overcome the liquid percolation threshold (Vigneresse et al. 1996), above which a continuous melt film is dispersed along solid fragment boundaries and above which intragrain melt pockets form, although their distribution will be constantly changing. This volume of melt is insufficient to fully lubricate the slip zone (and so does not measurably reduce the friction), so comminution and heating continue until melting is initiated within the next mineral phase that possesses the lowest fracture toughness and melting point: the feldspars (**Figure 9*c***). Because of their melt volume (40%), combined with melt from the mica, there is now sufficient melt to lubricate the interface (54% total); surviving fragments are dominated by a remaining volume of feldspars and the more refractory quartz. **Figure 8*b*** shows that in the case of Westerly granite, it is the melting of feldspar that controls the velocity-temperature evolution of the interface. The temperature of ~1100°C is the hinge point for change between velocity strengthening V_s and velocity weakening V_w responses. Below this temperature, the sliding interface is decelerated by the energy expended in comminution until a sufficient volume of friction melt is generated to lubricate the surface. Once this occurs, there is reduced friction, and the rate of deceleration decreases until cooling induces a return to brittle fracture. At that point, the sequence starts to repeat. This explains the loop shape in **Figure 8*a*** and can account for the presence of multiple generations of pseudotachylyte in a single slip zone (e.g., O'Hara 1992).

4.3. Microscopic Observations, Composition, and Viscosity

At the end of the experiment (3 s total duration), the two cylinder faces are "welded" together via the friction melt layer. A polished thin section was made of this interface. **Figure 10*a*** shows the friction melt zone, which is ~0.5 mm thick along its length. The bordering medium-grained wall-rock comprises quartz (darkest tone), feldspar (medium tones), biotite (bright tone and elongate grains in upper-left quadrant of image), and minor ilmenite (brightest tone). The friction melt zone comprises an aphanitic matrix (at this scale) and suspended clasts (mainly subangular quartz). **Figure 10*b*** shows that the surviving clasts are predominantly quartz, with smaller clasts of subordinate feldspar. This supports the hierarchy of melting based on the physical properties of the constituent minerals. **Figure 10*c*** reveals predominantly quartz clasts set in the matrix (one paler orthoclase is also present). Because of the narrow zone of friction melt, the matrix quenched to a glass (unlike most natural pseudotachylytes). Notable are the number of deformed bubbles within the matrix. Their number and distribution throughout the melt zone is too high for them to be derived solely from the breakdown of mica and the release of H_2O (as well as minor epidote and other hydrous phases). If biotite contains up to 4% water, then the 14% of mica in the protolith would yield only 0.6% water. This implies that most bubbles were formed primarily by cavitation within the liquid silicate matrix owing to high-speed flow. High-speed flow will also facilitate convective heating and thermal shock in surviving clasts (**Figure 10*d***). The preferential breakdown of biotite relative to the other mineral phases in Westerly granite is illustrated in **Figure 10*e***. Even though most of the matrix is glass in this experiment, some neocrystallization has occurred. **Figure 10*f*** shows ilmenite crystallites developed in the matrix close to a melting ilmenite clast. Their presence indicates that temperatures locally attained the melting point of $FeTiO_3$ (i.e., 1470°C) during the 2- to 3-second run.

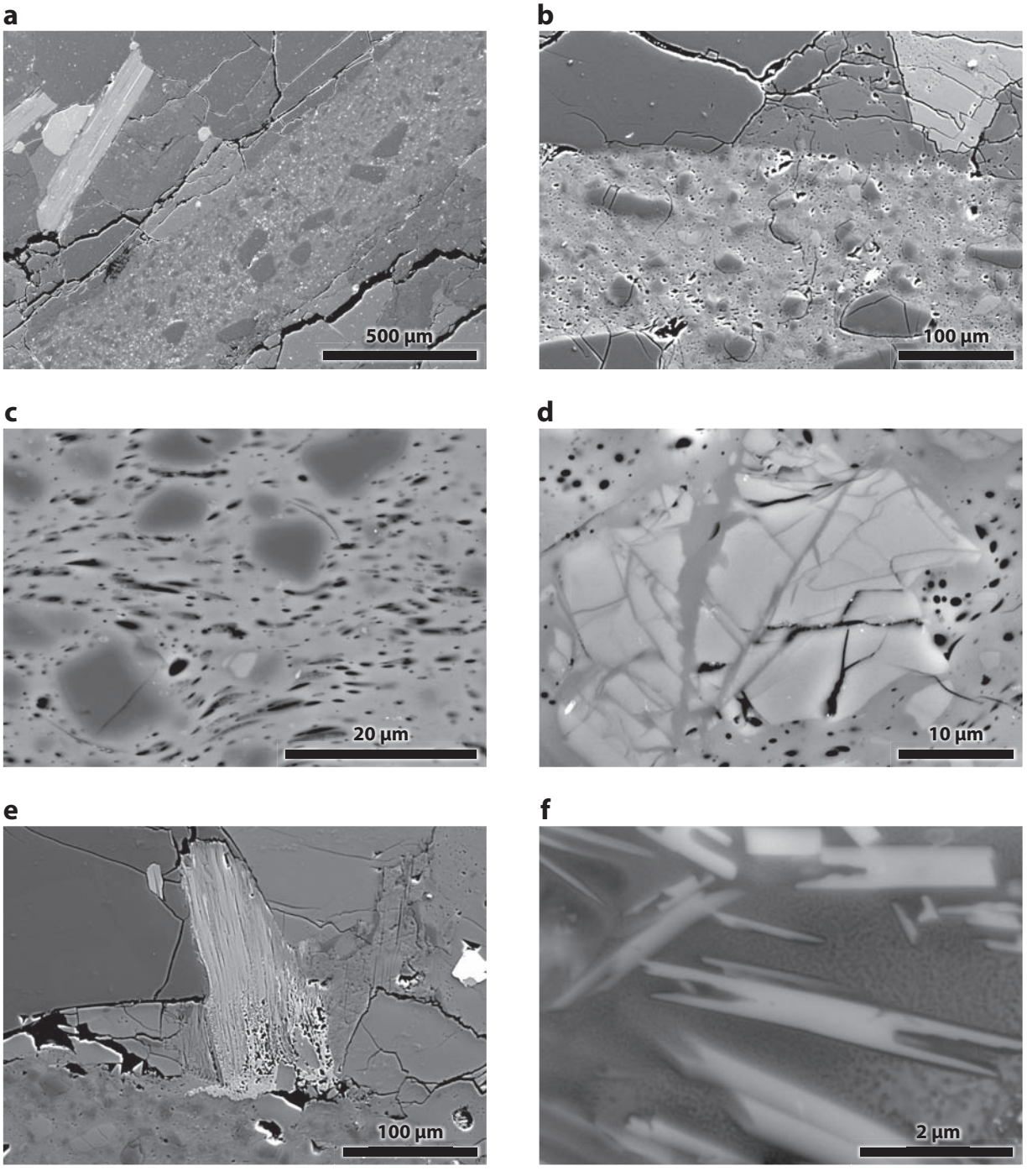

An important aspect of frictional melting is that it is selective. In the Westerly granite case study, because mica and feldspar have been preferentially melted, the matrix is relatively less siliceous and more ferromagnesian than the bulk rock, whereas the clasts are dominated by quartz and other more refractory accessory phases. This has implications for the viscosity of friction melt: Even if the protolith is considered acidic (granitic), the liquid component may be intermediate in composition. The bulk SiO_2 content of Westerly granite is 69% by weight, whereas the friction melt matrix yields 64% (Spray 1993). This difference can be larger for rocks possessing a higher proportion of hydrous ferromagnesian phases, such as mica and amphibole. Less siliceous matrices have lower viscosities. Coupled with the presence of bubbles, H_2O released from hydrous phases, and associated shear-thinning effects, the viscosities of crustal friction melts are typically comparable with those of alkaline and tholeiitic-basalt liquids (Spray 1993). This makes crustal friction melts good potential lubricants that allow faults to slide more easily.

5. PRODUCT REGIMES: THREE EXAMPLES

5.1. Seismogenic Faulting

Numerous descriptions of pseudotachylyte are associated with endogenic fault zones (see Lin 2008 for a recent summary), and its recognition and investigation have increased considerably over the past 20 years. The earlier descriptions of pseudotachylyte were in settings that facilitated contrast between medium- to light-colored host rocks (e.g., Archean gneisses) and black-matrix friction melts (e.g., **Figures 1** and **2**). This belies the fact that pseudotachylytes may be more common than suspected, especially in sedimentary rocks, where host rock and melt may be similarly colored and therefore difficult to distinguish.

Critically, interest in the development of friction melt along fault surfaces lies in the possibility of the melt lubricating the slip zone and thus modifying the system dynamics during an earthquake (e.g., Brodsky & Kanamori 2001, Spray 2005, Rice 2006, Beeler et al. 2008). In particular, it has been proposed that once slip exceeds a certain threshold, runaway rupture occurs (e.g., Kanamori & Heaton 2000). This might explain why the scaled energy for large earthquakes is 10 to 100 times larger than for small earthquakes (Brodsky & Kanamori 2001). Frictional melting may be facilitating this leap in scaled energy. **Figure 11** is a simplified model of the upper and part of the middle continental crust intersected by a sinistral strike-slip fault. The upper crust, which is shown ~11 km thick, contains weathering, diagenetic, and zeolite facies zones according to depth and the geothermal gradient (27°C km^{-1} in this example). The mechanical behavior of the upper crust is dominated by fracture toughness for all but the softest of minerals. Many shallow earthquakes nucleate within this zone (a common hypocenter depth is 10 km). It is an unstable zone with strain rates from 10^{-7} to 10^{5} s^{-1} (i.e., spanning the upper isothermal and lower adiabatic regimes). The transition to the middle crust occurs at ~300°C with the onset of plasticity in quartz and greenschist-facies metamorphic conditions. A further transition occurs at 450°C with the onset of feldspar plasticity and amphibolite-facies conditions. This zone is more stable with strain rates

Figure 10

Field emission electron microscope images of artificial pseudotachylyte generated from Westerly granite using axial friction-welding apparatus. (*a*) Overview of 500-μm wide vein. Note surviving quartz clasts. (*b*) Close-up of vein showing predominance of quartz clasts. (*c*) Flow structure in vesiculated glass (frozen melt) enclosing quartz clasts (single feldspar clast present just south of image center). Note distorted bubble structure. (*d*) Fragmenting feldspar clast "frozen" in place before complete breakup. (*e*) Breakdown and melting of biotite adjacent to friction melt and wallrock interface. Quartz to left of biotite and feldspar to right. (*f*) Several micron- to submicron-size ilmenite crystallites have grown in the melt (now glass).

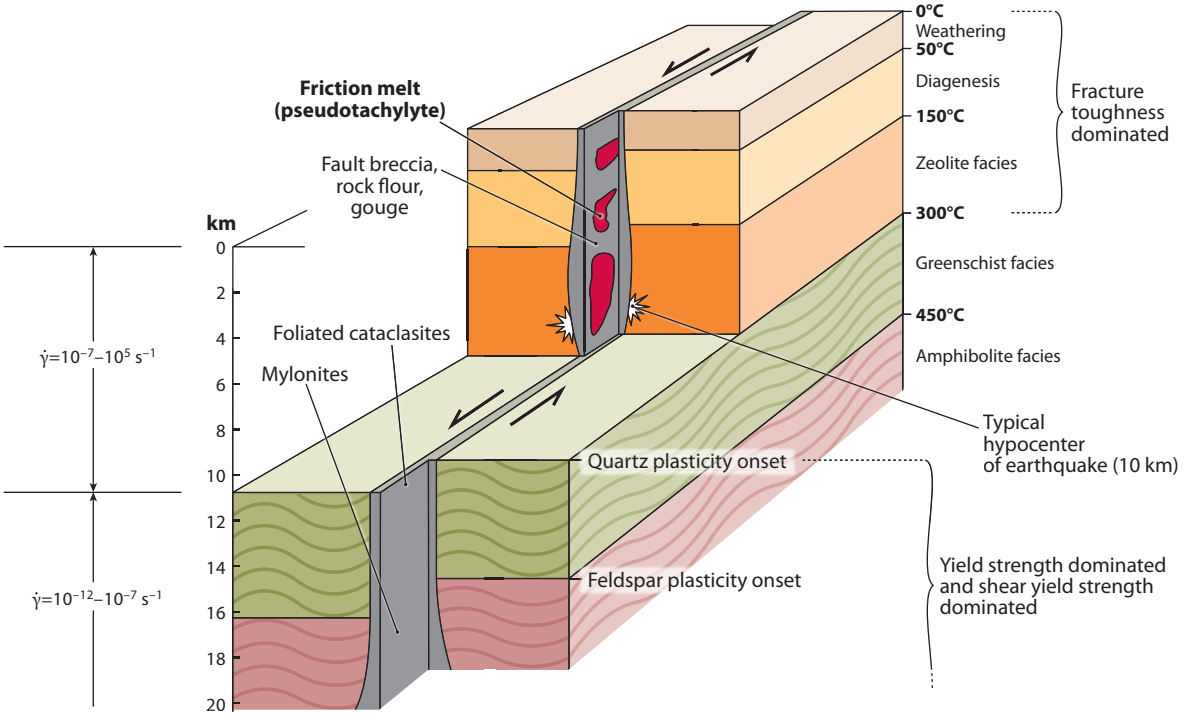

Figure 11

Model of a simple strike-slip zone developed in Earth's upper and middle continental crust. Fault/shear zone is shown in gray.

normally spanning 10^{-12} to 10^{-7} s^{-1}, well within the isothermal regime (**Figure 3**). The middle crust is yield strength and shear yield strength dominated. Traditional models of crustal faults show the faults moving by steady state (aseismic) creep in the middle crust and below, but intermittently (via earthquakes) in the upper crust. **Figure 11** shows the slip surfaces dominated by mylonites and foliated cataclasites in the middle crust, and fault breccia, gouge, and patches of friction melt in the upper crust. Many earthquakes initiate in the upper crust because of accumulated strain in the cooler, more brittle materials. It is possible for adiabatic conditions to prevail in the middle crust and below if higher strains are imposed: This would lead to transient discontinuities and failure initiation by ductile fracture (Sibson 1980). It is also possible for a rupture surface sourced at a hypocenter in the upper crust to penetrate the middle crust and thus impose high strain rates on a ductile regime and facilitate high-speed slip. Both scenarios could induce melting and promote the intermittent formation of friction melts within otherwise mylonitic host rocks (e.g., Swanson 2006). It has also been proposed that certain large-magnitude events occurring at mantle depths are accompanied by frictional melting (such as in the 637 km–deep, 8.3-magnitude Bolivian earthquake of 1994; Kanamori et al. 1998).

5.2. Impact Cratering

As indicated in the Introduction, the type area for pseudotachylyte occurs within a large terrestrial impact structure (Shand 1916). We now return to this setting to explore the nature of friction melts developed as a result of hypervelocity impact. Impact cratering is a violent, transient process

that achieves some of the highest known natural strain rates. This results in the partial and bulk melting and vaporization of solid targets, and even plasma generation (**Figure 3**). The impact process is customarily divided into three stages:

1. *contact*, when the asteroid or comet hits a planetary surface (typically at 15–25 km s^{-1} for meteorites) and generates a shock wave in both target and projectile;
2. *excavation*, when the momentum of the projectile removes material from a growing cavity in the target, creating melt, vapor, and solid ejecta; and
3. *modification*, when gravity reexerts influence and forces collapse of the cavity and uplift of the central core (at least for the larger craters).

We will not explore these processes in detail here; the reader is encouraged to read the appropriate literature (e.g., Melosh 1989, French 1998).

Pseudotachylyte and pseudotachylyte-like products are generated at different stages of the impact process. Shock veins are generated by shock wave–target interaction during the contact stage. These have been referred to as S-type (shock-type) pseudotachylytes (Spray 1998b), and are discussed in the next section. The pseudotachylyte that Shand described from Vredefort mainly comprises examples developed in slip zones that were generated during the gravitational adjustment of the transient cavity and surrounding crust. These have been referred to as E-type (endogenic-type) pseudotachylytes (Spray 1998b). E-type pseudotachylytes are generated in the same way that regular fault-related friction melts are made—by high-speed slip. However, the impact situation provides for some exceptional circumstances. Unlike most tectonic fault complexes (such as the San Andreas system), individual segments of which are, to a greater or lesser extent, pinned and unable to move freely (**Figure 12*a***), the collapse of impact-crater cavity margins results in large-scale unpinned movement (**Figure 12*b***). (The same can be said of certain landslides and caldera-collapse events.) When the single event displacement is >100 m, these movements have been referred to as superfaults (Spray 1997). If the slip surface is curviplanar and/or lumpy, lubrication via feedback between the friction melt and the coefficient of dynamic friction is prevented because new slip-surface obstacles are continually encountered. This can result in the generation of thick pseudotachylyte zones (tens to hundreds of meters wide). Displacement on terraces on the Moon can be on the order of several kilometers (**Figure 13*a***). The blanketing of these collapse structures by impact ejecta indicates that fault movement must have been completed in minutes (before ejecta return). Therefore, fault movement did not result from multiple, separate slip events occurring over protracted periods, but rather from single catastrophic slides. These scenarios can generate giant pseudotachylytes. One of the largest known is the South Range Breccia Belt of the Sudbury impact structure of Canada (Scott & Spray 2000). This friction melt zone is more than 45 km

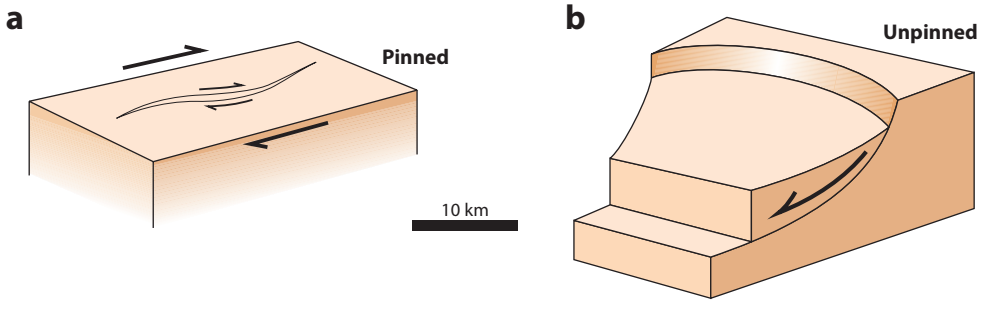

Figure 12

(*a*) Pinned fault segment in strike-slip setting. (*b*) Unpinned block slide in impact structure or landslide.

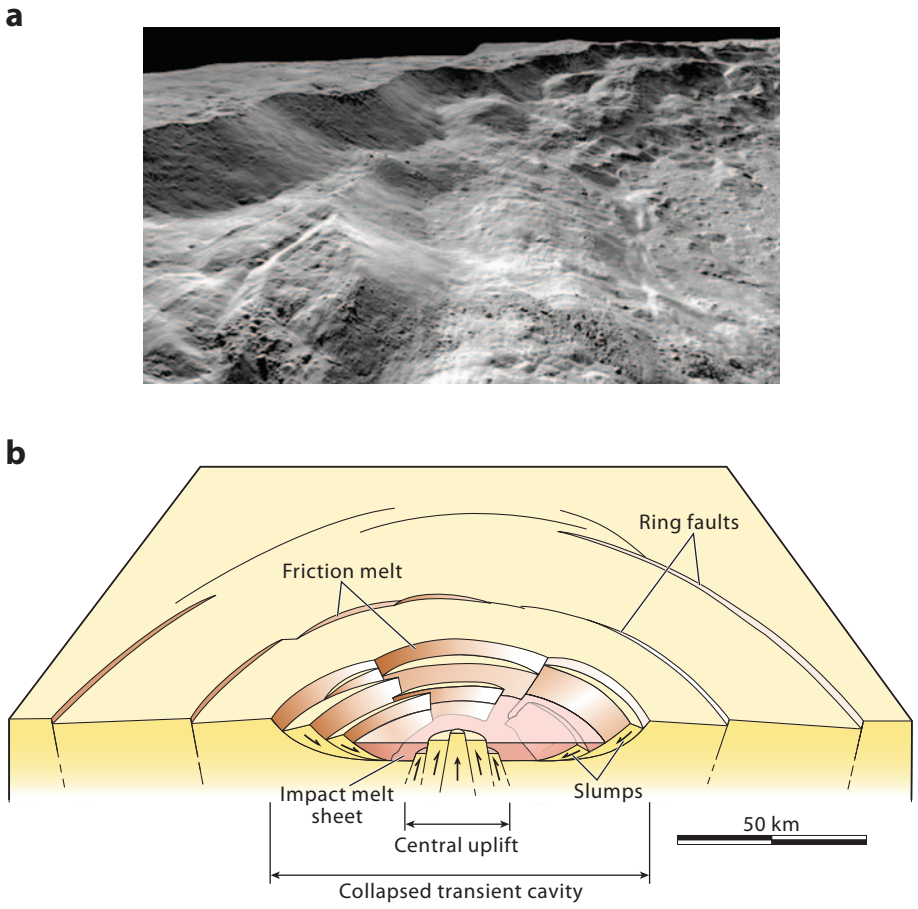

Figure 13

(*a*) Japanese Aerospace Exploration Agency's Kaguya lunar orbiter image of the collapsed transient cavity of the 85 km–diameter Tycho impact structure. This shows slump faulting and terrace formation with offsets of several kilometers. (*b*) Model of a complex impact structure showing fault systems that can generate giant friction melts.

long and up to 1 km wide (although it thins and thickens considerably along its length). It also hosts one of the largest Cu-Ni sulfide bodies in the world: the Frood-Stobie deposit, from which more than 600 million tons of ore have been extracted (Scott & Spray 1999). **Figure 13*b*** shows a model of a complex impact structure and the locations of large-displacement faults and associated friction melts. These are developed in three main regions: around the collapsed margins of the cavity, within the central uplift, and beyond the cavity as ring structures (Spray & Thompson 1995, Thompson & Spray 1996, Spray et al. 2004, Melosh 2005, Reimold & Gibson 2005). The central uplift is shown much simplified; the mechanism of formation of uplifts is not yet understood.

Recently, it has been proposed that some rocks previously considered pseudotachylyte in impact structures were derived by the injection of impact melt into impact-generated damage zones (Lieger et al. 2009). It can be difficult to distinguish impact melt from pseudotachylyte in the field; the two can coexist in the crater footwall or central uplift as dike-like bodies. The key is to carefully evaluate the chemistry of the rocks. Pseudotachylyte will tend to be more locally derived

(by the frictional melting of slip-zone wallrocks) and so will reflect local source compositions (although chemical differences between the pseudotachylyte matrix and entrained clasts must be borne in mind, as discussed in section 3.1). Impact melts are generated from a much larger volume of the target, so they will tend to possess compositions indicative of more regional-scale mixing and homogenization (especially for heterogeneous target terrains). With this approach, it has been possible to successfully distinguish dikes of pseudotachylyte (Thompson & Spray 1996) from dikes of impact melt (Tuchscherer & Spray 2002) within the Sudbury impact structure.

Determining the role of friction melts in facilitating the kilometer-scale movement of rock in impact structures is important: Most computer simulations invoke gross hydrodynamic behavior for the target (e.g., Goldin et al. 2006). There have been relatively few attempts at more realistically modeling cratering with partitioned deformation via discrete slip systems (e.g., O'Keefe et al. 2001, Senft & Stewart 2009).

5.3. Shock Veins in Meteorites and Impact Craters

Shock veins are narrow fracture-slip surfaces, typically less than 1 mm wide, that are common in some meteorites and terrestrial impact structures. Shock veins may contain high-pressure mineral polymorphs (e.g., coesite, stishovite, ringwoodite, majorite) that are generated under localized, significantly higher pressure and temperature conditions than those realized by the bulk material (e.g., Sharp & DeCarli 2006, Gillet et al. 2007). These shock excursions are considered to arise from shock-wave trapping and amplification mechanisms that are restricted to the veins (Spray 1999). In the context of frictional melting, shock veins are considered to be an extreme. **Figure 3** shows them occurring above strain rates of 10^6 s^{-1} as an extension of the normal pseudotachylyte field.

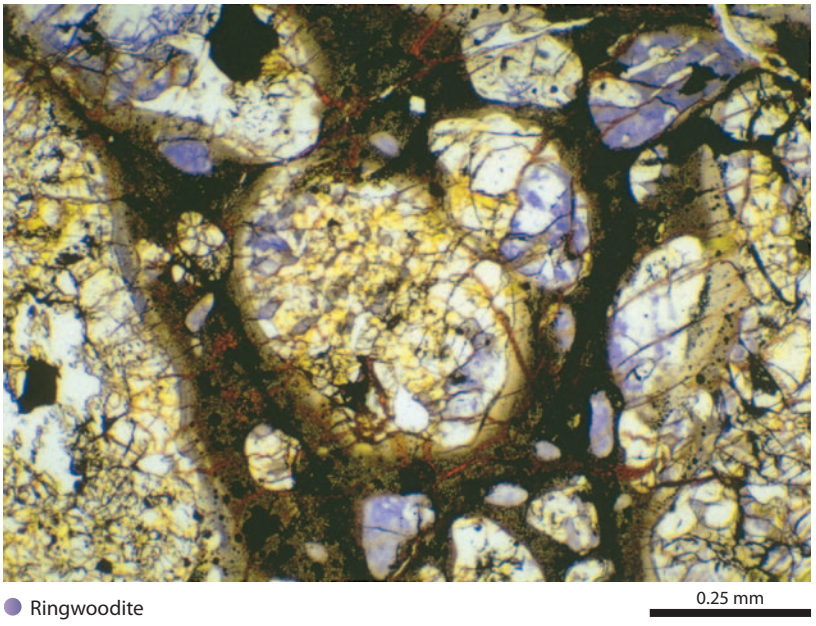

Figure 14

Plane-polarized light photomicrograph of a shock vein developed in the Catherwood L6 chondrite meteorite. Note the spinel-structured olivine polymorph ringwoodite, which is restricted to the veins and vein margins. Ringwoodite formation requires shock pressures of 20–25 GPa.

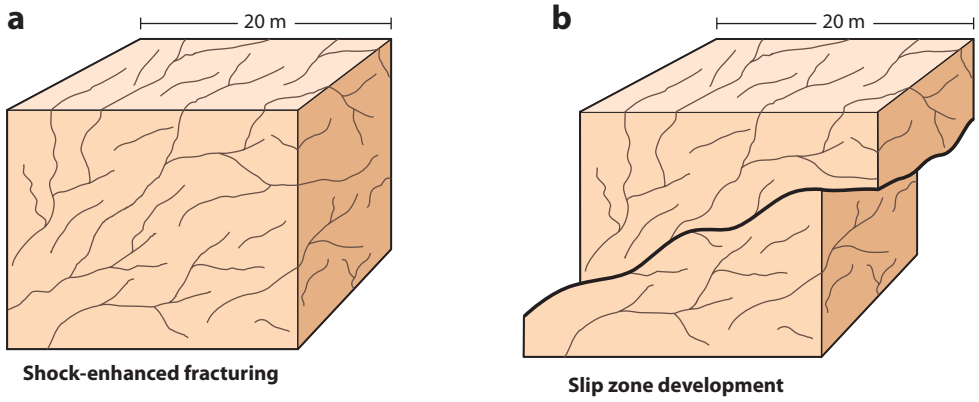

Figure 15

(*a*) Block showing pervasive shock veins (S-type pseudotachylyte) generated during shock-wave passage. (*b*) Subsequent exploitation of the weakened target rock facilitates slip and conventional (E-type) pseudotachylyte formation during the modification stage of the impact process.

Figure 14 is a photomicrograph of a 0.7 mm–wide shock vein developed in the Catherwood L6 chondrite. The distinctive blue phase is the high-pressure, spinel-structured, olivine polymorph ringwoodite, which does not occur outside the shock vein. Ringwoodite formation requires shock pressures of 20–25 GPa (Gillet et al. 2007). From Equation 1 we can determine that for a strain rate of 10^6 s^{-1} and a slip zone width of 0.7×10^{-3} m, the displacement (particle) velocity would have been 7 km s^{-1}, which is compatible with a typical shock-wave velocity of 15 km s^{-1}. At this speed, a unidirectional offset of 1 mm would occur in ~0.1 μs! This velocity is sufficient to melt the slip surface, despite the small offset. Melting occurs during shock loading, accompanied by frictional heating along microslip zones, and just after shock loading during pressure release: The combined temperature and pressure peak is sufficient to locally generate high-pressure mineral phases. S-type pseudotachylytes are therefore derived from a combination of friction and shock. The shock-induced fracturing and microfaulting of target rocks during hypervelocity impact (**Figure 15*a***) can predispose the material to failure during the subsequent gravity-driven modification stage and facilitate the generation of normal, ambient pressure (E-type) friction melts (**Figure 15*b***).

SUMMARY POINTS

1. Frictional melting in planetary materials occurs at high strain rates ($>10^{-2}$ s^{-1}) at slip velocities that exceed 0.1 m s^{-1}. The predominance of ceramic planetary materials and their intrinsic mechanical properties result in fracture toughness being a controlling element in comminution and adiabatic heating, which together lead to melting by friction.
2. There is a hierarchy of susceptibility to fracture and melting, which is dependent on mineral bonding and crystal structure. Soro- and phyllosilicates are the weakest, followed by double-chain inosilicates, single-chain inosilicates, tectosilicates, orthosilicates, and oxides.

3. High-speed rotary experiments have shown that frictional melting can result in the generation of low-viscosity liquids that can lubricate slip interfaces. Initial slip is velocity strengthening (comminution phase) followed slip weakening (melting phase), with possible cycling of these behaviors during a single slip event. The lubrication of faults by friction melt may facilitate large-magnitude earthquakes.
4. Friction melts (pseudotachylytes) constitute an important product of the impact-cratering process. Most of their occurrences equate with postshock, gravity-driven collapse and uplift tectonics. Chemical analysis may be required to distinguish some pseudotachylytes from impact melt in crater-floor and central-uplift settings, especially if both occur as dike-like bodies.
5. Shock veins are a special variant of pseudotachylyte that form at extreme strain rates by a combination of friction *and* shock during and immediately after the passage of the shock wave generated by a hypervelocity impact event.

FUTURE ISSUES

1. Additional detailed field mapping of exhumed pseudotachylyte-bearing crustal fault systems is required to better understand their three-dimensional distribution and structure. In particular, is slip accommodated on multiple displacement surfaces during coseismic slip, or on one primary failure plane?
2. We need to better define the role of faults and associated friction melts in facilitating the formation of impact-generated central uplifts and peak rings, and the collapse of transient cavities and outlier ring faults. This requires detailed three-dimensional field mapping of well-exposed impact structures.
3. Linking slip-zone macro- and microphysical phenomena to the seismic response is a major quest of the rock-mechanics and geophysics community. Currently, there is a disconnection between earthquake seismology and coseismic-slip mechanics.
4. Additional fracture-toughness determinations are required for the rock-forming minerals. This will help us better understand comminution in sliding silicate systems.
5. The formation of shock veins and the creation of extreme pressure-temperature excursions remain poorly understood. Future work should explore the physical interaction of shock and rarefaction waves with heterogeneous polyphase solids.

DISCLOSURE STATEMENT

The author is not aware of any affiliations, memberships, funding, or financial holdings that might be perceived as affecting the objectivity of this review.

ACKNOWLEDGMENTS

This research has been supported by the Natural Sciences and Engineering Research Council of Canada, the Canada Research Chairs program, the Canada Foundation for Innovation, and the University of New Brunswick. Thanks to Suporn Boonsue for assistance with field

emission electron microscopy and Norman Sleep for constructive comments. Discussions, field trips, and collaborations with a number of valued colleagues over the years have contributed to my understanding of frictional melting: Simon Kelley, Kieran O'Hara, Robert Maddock, Jerry Magloughlin, Jay Melosh, Uwe Reimold, Mark Swanson, and Lucy Thompson. Planetary and Space Science Centre contribution 65.

LITERATURE CITED

Ashby MF, Jones DRH. 2005a. *Engineering Materials 2*. Amsterdam: Elsevier. 451 pp. 3rd ed.

Ashby MF, Jones DRH. 2005b. *Engineering Materials 1*. Amsterdam: Elsevier. 448 pp. 3rd ed.

Atkinson BK. 1984. Subcritical crack growth in geological materials. *J. Geophys. Res.* 89:4077–114

Bailey EB, Maufe HB. 1960. *The Geology of Ben Nevis and Glen Coe and the Surrounding Country*. Geol. Surv. Great Britain, London: Her Majesty's Stationery Office. 307 pp.

Beeler NM. 2006. Inferring earthquake source properties from laboratory observations and the scope of lab contributions to source physics. In *Earthquakes: Radiated Energy and the Physics of Faulting*, ed. R Abercrombie, A McGarr, G Di Toro, H Kanamori, *Geophys. Monogr.* 170:99–119. Washington, DC: Am. Geophys. Union

Beeler NM, Tullis TE, Goldsby DL. 2008. Constitutive relationships and physical basis of fault strength due to flash heating. *J. Geophys. Res.* 113:B01401

Beke B. 1964. *Principles of Comminution*. Budapest: Akadémiai Kiadó. 163 pp.

Bell TH, Etheridge MA. 1973. Microstructures of mylonites and their descriptive terminology. *Lithos* 6:337–48

Biegel RL, Sammis CG, Dieterich JH. 1989. The frictional properties of a simulated gouge having a fractal particle distribution. *J. Struct. Geol.* 11:827–46

Bowden FP, Tabor D. 1950. *The Friction and Lubrication of Solids*. Part 1. Oxford: Clarendon. 337 pp.

Bradt RC, Newnham RE, Biggers JV. 1973. The toughness of jade. *Am. Mineral.* 58:727–32

Brodsky EE, Kanamori H. 2001. Elastohydrodynamic lubrication of faults. *J. Geophys. Res.* 106:16357–74

Broz ME, Cook RF, Whitney DL. 2006. Microhardness, toughness, and modulus of Mohs scale minerals. *Am. Mineral.* 91:135–42

Chester JS, Chester FM, Kronenberg AK. 2005. Fracture surface energy of the Punchbowl Fault, San Andreas system. *Nature* 437:133–36

Clauser C, Huenges E. 1995. Thermal conductivity of rocks and minerals. In *Rock Physics and Phase Relations: A Handbook of Physical Constants*, ed. TJ Ahrens, pp. 105–26. Washington, DC: Am. Geophys. Union

Clough CT. 1888. *The Geology of the Cheviot Hills (English Side). Explanation of Quarter Sheet 108 N.E., New Series, Sheet 5*. Mem. Geol. Surv. England and Wales, London: Her Majesty's Stationery Office. 60 pp.

Clough CT, Maufe HB, Bailey EB. 1909. The cauldron-subsidence of Glen Coe and the associated igneous phenomena. *Q. J. Geol. Soc. London* 65:611–78

Davidge RW. 1979. *Mechanical Behavior of Ceramics*. Cambridge, UK: Cambridge Univ. Press. 165 pp.

Deer WA, Howie RA, Zussman J. 1992. *An Introduction to the Rock-Forming Minerals*. Harlow, UK: Longman. 696 pp.

Di Toro G, Hirose T, Nielsen S, Pennacchioni G, Shimamoto T. 2006a. Natural and experimental evidence of melt lubrication of faults during earthquakes. *Science* 311:647–49

Di Toro G, Hirose T, Nielsen S, Shimamoto T. 2006b. Relating high-velocity rock-friction experiments to coseismic slip in the presence of melts. In *Earthquakes: Radiated Energy and the Physics of Faulting*, ed. R Abercrombie, A McGarr, G Di Toro, H Kanamori, *Geophys. Monogr.* 170:121–34. Washington, DC: Am. Geophys. Union

Earth Impact Database. 2009. **http://www.unb.ca/passc/ImpactDatabase/** (Accessed: 14/July/2009)

Erismann Th, Heuberger H, Preuss E. 1977. Der Bimsstein von Köfels (Tirol), ein Bergsturtz-"Friktionit." *Tschermaks Mineral. Petrogr. Mitt.* 24:67–119

Fettes DJ, Mendum JR, Smith DI, Watson JV. 1992. *Geology of the Outer Hebrides*. Mem. British Geol. Surv. London: Her Majesty's Stationery Office. 197 pp.

Fletcher MJ. 1972. *Friction Welding*. London: Mills & Boon. 67 pp.

French BM. 1998. *Traces of Catastrophe: A Handbook of Shock-Metamorphic Effects in Terrestrial Meteorite Impact Structures*. LPI Contrib. No. 954, Lunar Planet. Inst., Houston. 120 pp.
Gillet P, El Goresy A, Beck P, Chen M. 2007. High-pressure mineral assemblages in shocked meteorites and shocked terrestrial rocks: mechanisms of phase transformations and constraints on pressure and temperature histories. *Geol. Soc. Am. Spec. Pap.* 421:57–82
Goldin TJ, Wunnemann K, Melosh HJ, Collins GS. 2006. Hydrocode modeling of the Sierra Madera impact structure. *Meteorit. Planet. Sci.* 41:1947–58
Green DJ. 1998. *An Introduction to the Mechanical Properties of Ceramics*. Cambridge, UK: Cambridge Univ. Press. 336 pp.
Hagan JT. 1981. Impossibility of fragmenting small particles: brittle-ductile transition. *J. Mater. Sci.* 16:2909–11
Hartmann WK. 1969. Terrestrial, lunar, and interplanetary rock fragmentation. *Icarus* 10:201–13
Hirose T, Shimamoto T. 2003. Fractal dimension of molten surfaces as a possible parameter to infer the slip-weakening distance of faults from natural pseudotachylytes. *J. Struct. Geol.* 25:1560–74
Hodge HC, McKay JH. 1934. The "microhardness" of minerals comprising the Mohs scale. *Am. Mineral.* 19:161–68
Holland TH. 1900. The charnockite series, a group of Archaean hypersthenic rocks in peninsula India. *Mem. Geol. Surv. India* 28(Part 2):119–249
Horai K. 1971. Thermal conductivity of rock-forming minerals. *J. Geophys. Res.* 76:1278–308
Imber J, Strachan RA, Holdsworth RE, Butler CA. 2002. The initiation and early tectonic significance of the Outer Hebrides Fault Zone, Scotland. *Geol. Mag.* 139:609–19
Kanamori H, Heaton TH. 2000. Microscopic and macroscopic physics of earthquakes. *Geophys. Monogr.* 120:147–63. Washington, DC: Am. Geophys. Union
Kanamori H, Anderson DL, Heaton TH. 1998. Frictional melting during the rupture of the 1994 Bolivian earthquake. *Science* 279:839–42
Kelley SP, Reddy SM, Maddock R. 1994. Laser-probe $^{40}Ar/^{39}Ar$ investigation of a pseudotachylyte and its host rock from the Outer Isles thrust, Scotland. *Geology* 22:443–46
Kendall K. 1978. The impossibility of comminuting small particles by compression. *Nature* 272:710–11
Kennedy LA, Spray JG. 1992. Frictional melting of sedimentary rock during high-speed diamond drilling: an analytical SEM and TEM investigation. *Tectonophysics* 204:323–37
Killick AM. 1990. Pseudotachylyte generated as a result of drilling "burn-in." *Tectonophysics* 171:221–27
King W, Foote RB. 1865. On the geological structure of portions of the districts of Trichinopoly, Salem and South Arcot, Madras. *Mem. Geol. Surv. India* 4:223–377
Kipp ME, Grady DE, Chen EP. 1980. Strain-rate dependent fracture initiation. *Int. J. Fract.* 16:471–78
Knieke C, Sommer M, Peukert W. 2009. Identifying the apparent and true grinding limit. *Powder Tech.* 195:25–30
Knoop F, Peters CG, Emerson WB. 1939. Sensitive pyramidal-diamond tool for indentation measurements. *U.S. Natl. Bur. Stand.* Res. Pap. RP1220:39–61
Kokelaar P. 2007. Friction melting, catastrophic dilation and breccia formation along caldera superfaults. *J. Geol. Soc. London* 164:751–54
Lapworth C. 1885. The highland controversy in British geology: its causes, course and consequences. *Nature* 32:558–59
Lieger D, Riller U, Gibson RL. 2009. Generation of fragment-rich pseudotachylite bodies during central uplift formation in the Vredefort impact structure, South Africa. *Earth Planet. Sci. Lett.* 279:53–64
Lin A. 2008. *Fossil Earthquakes: The Formation and Preservation of Pseudotachylytes*. Berlin: Springer. 348 pp.
Lin A, Shimamoto T. 1998. Selective melting processes as inferred from experimentally generated pseudotachylytes. *J. Asian Earth Sci.* 6:533–45
Lind D, Sanders SP. 2004. *The Physics of Skiing*. New York: Springer-Verlag. 266 pp.
Lowrison GC. 1974. *Crushing and Grinding*. Ohio: CRC. 286 pp.
Lynch AJ. 1977. *Mineral Crushing and Grinding Circuits*. New York: Elsevier. 342 pp.
MacCulloch J. 1819. *Description of the Western Isles of Scotland, Including the Isle of Man*, Vol. 1. Edinburgh, Scotland: Constable & Company. 587 pp.

MacPherson WR, Schloessin HH. 1982. Lattice and radiative thermal conductivity variations through high *p*, T polymorphic structure transitions and melting points. *Phys. Earth Planet. Int.* 29:58–68
Maddock RH. 1983. Melt origin of fault-generated pseudotachylytes demonstrated by textures. *Geology* 11:105–8
Magloughlin JF, Spray JG. 1992. Frictional melting processes and products in geological materials: introduction and discussion. *Tectonophysics* 204:197–206
Marone C. 1998. Laboratory-derived friction laws and their application to seismic faulting. *Annu. Rev. Earth Planet. Sci.* 26:643–96
Marone C, Scholz CH. 1989. Particle-size distribution and microstructures within simulated fault gouge. *J. Struct. Geol.* 11:799–814
Martini JEJ. 1978. Coesite and stishovite in the Vredefort Dome, South Africa. *Nature* 277:495–96
Mawer CD. 1986. What is a mylonite? *Geosci. Can.* 13:33–34
Melosh HJ. 1989. *Impact Cratering: A Geologic Process*. New York: Oxford. 245 pp.
Melosh HJ. 2005. The mechanics of pseudotachylite formation. In *Impact Tectonics*, ed. C Koeberl, H Henkel, pp. 55–80. Berlin: Springer
Meyers M. 1994. *Dynamic Behavior of Materials*. New York: Wiley-Interscience. 668 pp.
Meyers M, Chawla K. 2009. *Mechanical Behavior of Materials*. Cambridge, UK: Cambridge Univ. Press. 856 pp.
Mogi K. 1974. On the pressure dependence of strength of rocks and the Coulomb-fracture criterion. *Tectonophysics* 21:273–85
Mohs F. 1825. *Treatise on Mineralogy*. Edinburgh, Scotland: Caledonian Mercury. 458 pp.
Moore DE, Rymer MJ. 2007. Talc-bearing serpentinite and the creeping section of the San Andreas fault. *Nature* 448:795–97
O'Hara KD. 1992. Major- and trace-element constraints on the petrogenesis of a fault-related pseudotachylyte, western Blue Ridge province, North Carolina. *Tectonophysics* 204:279–88
O'Keefe JD, Stewart ST, Lainhart ME, Ahrens TJ. 2001. Damage and rock-volatile mixture effects on impact crater formation. *Int. J. Impact Eng.* 26:543–53
Passchier CW, Trouw AJ. 2005. *Microtectonics*. Berlin: Springer-Verlag. 366 pp.
Ravi-Chandar K, Knauss WG. 1984. An experimental investigation into dynamic fracture: I. Crack initiation and arrest. *Int. J. Fract.* 25:247–62
Ray SK. 2004. Melt-clast interaction and the power-law size distribution of clasts in pseudotachylytes. *J. Struct. Geol.* 26:1831–34
Reimold WU, Colliston WP. 1994. Pseudotachylites of the Vredefort Dome and the surrounding Witwatersrand Basin, South Africa. In *Large Meteorite Impacts and Planetary Evolution*, ed. BO Dressler, RAF Grieve, VL Sharpton, *Geol. Soc. Am. Spec. Pap.* 293:177–96
Reimold WU, Gibson RL. 2005. "Pseudotachylites" in large impact structures. In *Impact Tectonics*, ed. C Koeberl, H Henkel, pp. 1–53. Berlin: Springer
Rice JR. 2006. Heating and weakening of faults during earthquake slip. *J. Geophys. Res.* 111:B05311
Sammis CG, Ben-Zion Y. 2008. Mechanics of grain-size reduction in fault zones. *J. Geophys. Res.* 113:B02306
Sammis CG, Biegel R. 1989. Fractals, fault-gouge, and friction. *Pure Appl. Geophys.* 131:255–71
Sammis CG, King GCP. 2007. Mechanical origin of power law scaling in fault zone rock. *Geophys. Res. Lett.* 34:L04312
Sammis CG, King GCP, Biegel R. 1987. The kinematics of gouge deformation. *Pure Appl. Geophys.* 125:777–812
Scholz CH. 2002. *Mechanics of Earthquakes and Faulting*. Cambridge, UK: Cambridge Univ. Press. 471 pp.
Scott RG, Spray JG. 1999. Magnetic fabric constraints on friction melt flow regimes and ore emplacement direction within the South Range Breccia Belt, Sudbury impact structure. *Tectonophysics* 307:163–89
Scott RG, Spray JG. 2000. The South Range Breccia Belt of the Sudbury impact structure: a possible terrace collapse feature. *Meteorit. Planet. Sci.* 35:505–20
Senft LE, Stewart ST. 2009. Dynamic fault weakening and the formation of large impact craters. *Earth Planet. Sci. Lett.* 287:471–82
Shand SJ. 1916. The pseudotachylyte of Parijs (Orange Free State), and its relation to "trap-shotten gneiss" and "flinty crush-rock." *Q. J. Geol. Soc. London* 72:198–21

Sharp TG, DeCarli PS. 2006. Shock effects in meteorites. In *Meteorites and the Early Solar System II*, ed. DS Lauretta, HY McSween, pp. 653–77. Tucson: Univ. Ariz. Press
Shimamoto T, Tsutsumi T. 1994. A new rotary-shear high-speed frictional testing machine: its basic design and scope of research. *J. Tecton. Res. Group Jpn.* 39:65–78 (In Japanese with English abstract)
Sibson RH. 1975. Generation of pseudotachylyte by ancient seismic faulting. *Geophys. J. R. Astron. Soc.* 43:775–94
Sibson RH. 1980. Transient discontinuities in ductile shear zones. *J. Struct. Geol.* 2:165–71
Snoke AW, Tullis J, Todd VR, eds. 1998. *Fault-Related Rocks: A Photographic Atlas*. Princeton, New Jersey: Princeton Univ. Press. 617 pp.
Spray JG. 1987. Artificial generation of pseudotachylyte using friction welding apparatus: simulation of melting on a fault plane. *J. Struct. Geol.* 9:49–60
Spray JG. 1988. Generation and crystallization of an amphibolite shear melt: an investigation using radial friction welding apparatus. *Contrib. Mineral. Petrol.* 99:464–75
Spray JG. 1989. Slickenside formation by surface melting during the mechanical excavation of rock. *J. Struct. Geol.* 11:895–905
Spray JG. 1992. A physical basis for the frictional melting of some rock-forming minerals. *Tectonophysics* 204:205–21
Spray JG. 1993. Viscosity determinations of some frictionally generated silicate melts: implications for fault zone rheology at high strain rates. *J. Geophys. Res.* 98(B5):8053–68
Spray JG. 1995. Pseudotachylyte controversy: Fact or friction? *Geology* 23:1119–22
Spray JG. 1997. Superfaults. *Geology* 25:305–8
Spray JG. 1998a. Pseudotachylyte type area: the Vredefort Structure, South Africa. In *Fault-Related Rocks: A Photographic Atlas*, ed. AW Snoke, J Tullis, VR Todd, pp. 76–79. Princeton, New Jersey: Princeton Univ. Press
Spray JG. 1998b. Localized shock- and friction-induced melting in response to hypervelocity impact. In *Meteorites: Flux with Time and Impact Effects*, ed. MM Grady, R Hutchinson, GJH McCall, DA Rothery, pp. 171–80. *Geol. Soc. London Spec. Pub.* 140:171–80
Spray JG. 1999. Shocking rocks by cavitation and bubble implosion. *Geology* 27:695–98
Spray JG. 2005. Evidence for melt lubrication during large earthquakes. *Geophys. Res. Lett.* 32:L070301
Spray JG, Butler HR, Thompson LM. 2004. Tectonic influences on the morphometry of the Sudbury impact structure: implications for terrestrial cratering and modeling. *Meteorit. Planet. Sci.* 39:287–301
Spray JG, Thompson LM. 1995. Friction melt distribution in a multi-ring impact basin. *Nature* 373:130–32
Suresh S, Nakamura T, Yeshurun Y, Yang K-H, Duffy J. 1990. Tensile fracture toughness of ceramic materials: effects of dynamic loading and elevated temperatures. *J. Am. Ceram. Soc.* 73:2457–66
Swanson MT. 2006. Pseudotachylyte-bearing strike-slip faults in mylonitic host rocks, Fort Foster Brittle Zone, Kittery, Maine. In *Earthquakes: Radiated Energy and the Physics of Faulting*, ed. R Abercrombie, A McGarr, G Di Toro, H Kanamori, *Geophys. Monogr.* 170:167–79. Washington, DC: Am. Geophys. Union
Tabor D. 1954. Mohs's hardness scale—a physical interpretation. *Proc. Phys. Soc. Sect. B* 67:249–57
Taylor EW. 1949. Correlation of the Mohs's scale of hardness with the Vicker's hardness numbers. *Mineral. Mag.* 28:718–21
Teall JJH. 1918. Dynamic metamorphism; a review, mainly personal. *Proc. Geol. Assoc. London* 29:1–15
Thompson LM, Spray JG. 1996. Pseudotachylyte petrogenesis: constraints from the Sudbury impact structure. *Contrib. Mineral. Petrol.* 125:359–74
Tromans D. 2008. Mineral comminution: energy efficiency considerations. *Miner. Eng.* 21:613–20
Tromans D, Meech JA. 2002. Fracture toughness and surface energies of minerals: theoretical estimates for oxides, sulphides, silicates and halides. *Miner. Eng.* 15:1027–41
Tsutsumi T, Shimamoto T. 1997. High-velocity frictional properties of gabbro. *Geophys. Res. Lett.* 24:699–702
Tuchscherer MG, Spray JG. 2002. Geology, mineralization, and emplacement of the Foy offset dike, Sudbury impact structure. *Econ. Geol.* 97:1377–97
Turcotte DL. 1992. *Fractals and Chaos in Geology and Geophysics*. Cambridge, UK: Cambridge Univ. Press. 221 pp.

Vigneresse JL, Barbey P, Cuney M. 1996. Rheological transitions during partial melting and crystallization with application to felsic magma segregation and transfer. *J. Petrol.* 37:1579–1600

Von Rittinger PR. 1867. *Lehrbuch der Aufbereitungs Kunde*. Berlin: Ernst & Korn. 110 pp.

Wenk H-R. 1978. Are pseudotachylites products of fracture or fusion? *Geology* 6:507–11

White SH. 1973. Syntectonic recrystallization and texture development in quartz. *Nature* 244:276–78

Whitney DL, Broz M, Cook RF. 2007. Hardness, toughness, and modulus of some common metamorphic minerals. *Am. Mineral.* 92:281–88

Wilczek M, Bertling J, Hintemann D. 2004. Optimised technologies for cryogenic grinding. *Int. J. Miner. Process.* 74S:S425–34

Yund RA, Blanpied ML, Tullis TE, Weeks JD. 1990. Amorphous material in high strain experimental fault gouges. *J. Geophys. Res.* 95:15589–602

Zhang SW. 2004. *Tribology of Elastomers*. Amsterdam: Elsevier. 282 pp.

Annual Review
of Earth and
Planetary Sciences

Volume 38, 2010

Contents

Indexes

Errata

An online log of corrections to *Annual Review of Earth and Planetary Sciences* articles may be found at http://earth.annualreviews.org